1

R- JUL 22 2004

AFRL-SR-AR-TR-04-
0406

REPORT DOCUMENTATION PAGE

1. REPORT DATE *(DD-MM-YYYY)* 06/18/2004	**2. REPORT TYPE** Final Report	**3. DATES COVERED** *(From - To)* Nov. 2000 – Nov. 2003

4. TITLE AND SUBTITLE Turbulence and Complex Flow Phenomena in Axial Turbomachines	**5a. CONTRACT NUMBER**
	5b. GRANT NUMBER F49620–01–1–0010
	5c. PROGRAM ELEMENT NUMBER
6. AUTHOR(S) Katz, Joseph and Meneveau, Charles	**5d. PROJECT NUMBER**
	5e. TASK NUMBER
	5f. WORK UNIT NUMBER
7. PERFORMING ORGANIZATION NAME(S) AND ADDRESS(ES) The Johns Hopkins University Department of Mechanical Engineering 3400 N. Charles St. Baltimore, MD 21218	**8. PERFORMING ORGANIZATION REPORT**
9. SPONSORING / MONITORING AGENCY NAME(S) AND ADDRESS(ES) Air Force Office of Scientific Research 801 North Randolph Street Arlington VA, 22203-1977	**10. SPONSOR/MONITOR'S ACRONYM(S)** AFOSR/NA
	11. SPONSOR/MONITOR'S REPORT NUMBER(S)

12. DISTRIBUTION / AVAILABILITY STATEMENT

Approved for public release;
distribution unlimited.

20040810 018

13. SUPPLEMENTARY NOTES

14. ABSTRACT

The objective of this project is to measure the unsteady flow in axial turbomachines and use the data to address turbulence and complex flow modeling issues. The measurements are performed in an optically index matched facility, which allows unobstructed 2-D and Stereo PIV measurements within an entire stage. The data provide unprecedented insight on blade-blade, blade–wake, wake-boundary layer and wake–wake interactions in the hub, mid-span and tip regions. Turbulence and unsteady flow phenomena are investigated at three levels: Passage-averaged steady RANS, unsteady RANS, and LES. Data analysis provides the distributions of deterministic Reynolds and sub-grid stresses, deterministic and turbulent kinetic energy, turbulence production and dissipation, as well as energy exchange between the average passage flow, the turbulence at different scales, and the deterministic energy.

15. SUBJECT TERMS

Particle Image Velocimetry, turbomachines, Deterministic Stresses, Turbulence, wake-wake interactions, wake-blade interactions

16. SECURITY CLASSIFICATION OF:			**17. LIMITATION OF ABSTRACT**	**18. NUMBER OF PAGES**	**19a. NAME OF RESPONSIBLE PERSON**
a. REPORT U	**b. ABSTRACT** U	**c. THIS PAGE** U	UU		**19b. TELEPHONE NUMBER** *(include area code)* 410-516-5470

8-4-04

BEST AVAILABLE COPY

Turbulence and Complex Flow Phenomena in Axial Turbomachines

Final Report

Submitted By

Joseph Katz and Charles Meneveau

Department of Mechanical Engineering
The Johns Hopkins University
Baltimore, MD 21218

This project was sponsored by the Air Force Office of Scientific Research under grant No. F49620 – 01 – 1 – 0010. The program manager is T. Beutner.

1.0 Executive summary

The objective of this project is to measure the unsteady flow in axial turbomachines and use the data to address turbulence and complex flow modeling issues that are specific to such complex environments. The research was funded under AFOSR grant # F49620 – 01 – 1 – 0010. This report introduces and subsequently analyzes data obtained in a unique two-stage axial-turbomachine flow visualization facility, which allows unobstructed view on the flow within an entire turbomachines stage. This facility contains fluid (concentrated solution of NaI in water) that matches the optical index of refraction of the acrylic rotor and stator blades. Two and three dimensional velocity measurements have been performed using 2-D PIV (Particle Image Velocimetry) and Stereo PIV. The measurements cover the entire stage, several spanwise planes, many phases and varying magnifications. They provide insight on the complex flow associated with blade-blade, blade–wake, wake-boundary layer and wake–wake interactions within multi-stage turbomachines at unprecedented levels of detail.

Turbulence and unsteady flow phenomena have been investigated at three distinct levels of modeling:

Passage-averaged, steady RANS (Adamczyk, 1985), presently used for multiple blade-row simulations. We measure the distributions of deterministic stresses, examine the evolution of deterministic kinetic energy, and determine the extent of energy exchange between the average passage flow, the turbulence and the deterministic energy. In the tip vortex region the deterministic kinetic energy is particularly high, requiring a focused modeling effort and additional measurements.

In the context of unsteady RANS, We measure the distributions of Reynolds stresses and turbulence kinetic energy, and examine the effects of wake-blade and wake-wake interactions on the structure, production and dissipation of turbulence. The phase-averaged Reynolds stresses over the entire stage demonstrate that the flow consists of a lattice of interacting wakes. Turbulence spectra enable us to estimate and compare the dissipation to the production rates. Comparisons between magnitudes, trends and alignments of stresses and strain rates identify regions of potential problems in Reynolds stress modeling. For example, non-uniformities generated by upstream blade rows kinks the rotor wake and generate regions with high turbulence, concentrated vorticity and a complex strain structure. Impingement of a wake on a blade alters the boundary layer, making it thinner. The extensive database has been made available to the CFD community for code validation.

In the context of LES, spatial filtering of the data enables direct measurements of subgrid-scale (SGS) stresses and evaluation of fluxes of kinetic energy across different scales. The analysis also examines the energy flux from the (resolved and subgrid) mean flow to the resolved and subgrid turbulence.

The experimental results obtained to-date have already been published in five journal papers (Chow et al., 2002a, 2003a; Uzol et al., 2002a, b, 2003a), and ten conference papers (Chow et al., 2002b, c, 2003b, c; Uzol et al., 2001, 2002c, 2003b, 2004a, b; Soranna et al., 2004). An additional journal paper (Meneveau and Katz, 2002) introduces a new deterministic stress model. The complete list is provided in Section 6.

The background and scientific objectives of this project are presented in Section 2. Section 3 describes the optically index-matched, axial turbomachine, flow visualization facility. Section 4 presents sample data and results of analysis on the three levels of modeling outlined above, with reference to publications that contain additional details. Future plans are outlined in Section 5.

2.0 Objectives and Scientific Motivation

Flows in turbomachines, i.e. compressors, turbines, and pumps, are three-dimensional, complex and unsteady. They dominate the performance, efficiency, noise, and vibrations of these machines, and as a result must be understood and accurately predicted. In this project we examine the turbulence and unsteady flow in turbomachines at three modeling levels:

(i) Passage-averaged, steady RANS;

(ii) Unsteady RANS;

(iii) Large-Eddy-Simulation (LES).

The "average-passage" RANS equations, introduced first by Adamczyk (1985), enable computations of time-averaged flows within multi-stage turbomachines, while using steady boundary conditions, but still accounting for blade-rows interactions. This approach is important as a practical design tool for turbomachines with multiple blade rows and varying number of rotor and stator blades in consecutive stages. In this formulation, each blade row has a steady average-passage flow field, which extends from the inlet to the exit of the machine. Neighboring blade rows are replaced with circumferentially uniform systems of body forces, energy sources and (not necessarily uniform) deterministic stresses (Adamczyk, 1986; Adamczyk et al., 1986, 1990; Rhie et al., 1998; LeJambre et al., 1998; Busby et al., 2000). The effects of phase-dependent unsteadiness on the average-passage flow field are accounted for through the deterministic stresses, which must be modeled in order to obtain a closed system of equations. Different models for the deterministic stresses have already been proposed (e.g. Adamczyk, 1986; Van de Wall 2000; Meneveau and Katz, 2002; He et al., 2002). However, unlike RANS closure models, there are no widely accepted and validated modeling tools. To develop such models one requires a database obtained either from experiments or from unsteady RANS involving multi stages. The latter approach introduces uncertainties related to turbulence closure models.

In previous experimental studies, the deterministic stresses have been obtained either by traversing single point sensors (e.g. Prato et al., 1997, 1998; Suryavamshi et al., 1998a, b), or by Particle Image Velocimetry (PIV) measurements in quasi 2-D centrifugal pumps (Sinha & Katz, 2000; Sinha et al., 2000). Implementation of PIV in multistage axial turbomachines is extremely difficult due to optical obstruction by the multiple, often twisted blades to the illuminating laser sheet and to the camera. Furthermore, reflections from boundaries significantly reduce the data quality in boundary layers. Consequently, most of the PIV data on flows within multistage axial turbomachines (Tisserant et al., 1997; Gogineni et al., 1997; Balzani et al., 2000; Wernet, 2000; Sanders et al., 2002) are limited to parts of the passages. In facilities involving compressible flows, these problems seem to be unavoidable. However, characterization of the interactions between blade rows, e.g. wake-wake, wake-blade, wake-boundary layer interactions, require a complete picture on the mean flow structure and turbulence, including the flow within boundary layers and very near wakes. To address these requirements we have constructed a facility that enables unobstructed optical access using transparent rotor and stator blades operating in a liquid, which has the same optical index of refraction as the blades. A brief description of this system is provided Section 3.

In Phase-averaged unsteady RANS two simulations of one or a few passages are performed, one in the rotor frame and the other in the stator frame of reference. They are coupled by unsteady boundary conditions arising from sweeping the outlet plane of one solution past the inlet plane of the other (see e.g. Rai, 1987; Lakshminarayana, 1991; Suryavamshi et al., 1998a; Ho and Lakshminarayana, 1995 and many others). This approach is currently limited to single-stage computations, since simulations of multi-stage configurations are prohibitive, especially when blade-counts vary from one stage to the next. Thus, it is believed that unsteady RANS of an entire multistage compressor is not on the horizon, justifying a continued interest in modeling issues of the passage-averaged technique. However, unsteady RANS can be used to provide data on the flow structure within a limited subsection of the turbomachine, much like experimental data. The main difficulty with unsteady RANS is the modeling of Reynolds stresses, which creates uncertainties about the validity of the results. Currently no consensus exists as to which of the many Reynolds stress models is best suited for turbomachine applications (Lakshminarayana, 1991). Although unsteady RANS modeling is not the primary focus of this project, still, we have mapped the spatial and temporal distribution of the unsteady flow structure and Reynolds stresses, along with the distributions of turbulence production and dissipation rates. These data are available for code validation and for evaluation of Reynolds stress models.

The primary difficulties in applications of RANS are caused by the fact that all the turbulence, including eddies with sizes comparable to an entire vane passage, must be modeled. Since these eddies do not have a universal structure (e.g. Wilcox, 1993; Speziale, 1991), it is necessary to adjust the models on a case-by-case basis, which reduces their effectiveness as a predictive tool. Consequently, to provide fundamentally more accurate simulations of turbulent flows in complex environment, it is of interest to explore the application of Large-Eddy simulations.

Large-Eddy-Simulation (LES) consists of solving the spatially filtered, unsteady Navier-Stokes equations (Rogallo & Moin, 1984, Lesieur & Metais, 1996; Meneveau & Katz, 2000). Thus, if applied to turbomachines, it will capture both the unsteadiness associated with relative motion between rotor and stator, and the large-scale turbulent eddies. A practical limitation of LES is its high cost of computations compared to RANS. However, rapid increases in computer power are raising the expectation that LES may soon become practical even in complex turbomachine environments. There has already been considerable effort in development of LES models and applications to various basic flows, and some of increasing complexity.

Our group has experimentally examined several issues related to SGS modeling in relatively simple flows, such as homogeneous turbulence (Meneveau, 1993), the far-field of a round jet

(Liu et al., 1994, 1995), in a cylinder wake (O'Neil & Meneveau, 1997), during rapid straining (Liu et al., 1999, Chen et al., 2004), and within a square duct (Zhang et al., 1997, Tao et al., 2000, 2002). We have also examined the structure of SGS stresses and dissipation for complex flows in centrifugal pumps (Sinha et al., 2000a, b). Considerable portion of this effort has involved implementation of 2-D and holographic PIV to generate the databases and some of the analysis has been based on hot wire data. As reviewed in Meneveau & Katz (2000), the basic modeling paradigm that has been established by our work is the use of computed large-scales to locally guide the modeling at small scales. We learned from simpler flows that model coefficients must be modified when turbulence is exposed, for example, to rapid straining or when the filter scale approaches the integral scale. The available data indicates that such modifications can be determined from the response of the resolved structures to the local flow. LES, unlike RANS, allows us to perform "dynamic" modifications to the modeling, since part of the turbulence is resolved. When applying LES to the unsteady flow in a blade-passage, there is a need to implement much more refined models to account for different flow regimes.

Addressing modeling issues at the three levels outlined in this section requires an extensive database. Thus, our initial effort has focused on obtaining a complete data set on the distributions and dynamics of deterministic stresses over an entire stage of an axial turbomachine. As demonstrated in section 4, the data provide an unparalleled insight on the complex lattice of interacting turbulent wakes within the stage. In the context of passage-average simulations, the results enable us to prioritize our modeling effort, for example, to a tip vortex interacting with a stator blade. In the context of unsteady RANS, we provide data on the distributions of turbulent kinetic energy, production and dissipation rates associated with wake-wake and wake-blade interactions. In the context of LES, we have measured the spatial distributions of SGS stresses, and are presently in the process of examining the energy flux across different scales. The results provide insight on the effect of implementing LES using spatial filters with scales that are smaller, but are of the same order of magnitudes as the width of wakes.

3. Test Facility, Experimental Setup and Procedures.

3.1 The Index-Matched Axial Turbomachine Facility

The axial turbomachine test facility enables us to perform detailed and unobstructed PIV measurements at any point within an entire stage at varying magnifications, near and away from blades. To generate such data using optical techniques one needs an unobstructed view of the entire domain. This unlimited optical access is facilitated using transparent (acrylic) rotors and stators that have the same optical index of refraction as the working fluid, a concentrated solution, 62%-64% by weight, of NaI in water. This fluid has a specific gravity of 1.8 and a kinematic viscosity of 1.1×10^{-6} m^2/s, i.e. very close to that of water. Thus, the blades become almost invisible, do not obstruct the field of view and do not alter the direction of the illuminating laser sheet required for PIV measurements. Information related to use and maintain the NaI solutions can be found in Uzol et al. (2001, 2002a).

The index-matched facility was constructed using funding provided in part by AFOSR and in part by ONR. An overview of the system is presented in Figure 1. Two different test setups have been utilized (Figure 2). Setup No. 1, manufactured with AFOSR funding, has been used for examining blade-row interactions in multistage turbomachines, including the detailed analysis of deterministic stresses discussed in this proposal. It has 4 blade rows constituting two identical stages, and a window, which covers the entire second stage. The main geometrical parameters of this axial-turbo-pump are listed in Table 1. Additional relevant parameters are a rotor blade thickness of 7.62 mm, and camber varying from 2.54 mm at the hub to 1.98 mm at the tip. The stator's blade thickness is 11 mm and its camber is 6.22 mm. The gap between the rotor and the stator is 50 mm. The Reynolds number based on the tip speed and rotor chordlength is 3.7×10^5 at 500 rpm, the speed of the present tests.

The system is driven by a 25 HP rim-driven motor, which drives the first rotor directly. The two rotors are connected by a common shaft, supported by precision bearings, with variable length to vary the gap between blade rows. The facility is temperature controlled and supports other devices including pressure transducers, honeycombs and grids. It also allows modifications of elements and gaps between blade rows. A precision shaft encoder and a control system are used for synchronizing our PIV system with the rotor phase. Optical access is provided by a window that extends from upstream of the rotor, covers the entire second stage and terminates downstream of the stator (Figures 2 and 3). A window located at the corner of the facility provides an unobstructed view in the axial direction. An additional transparent insert enables us to introduce a probe containing the laser-sheet optics (Figure 3. Consequently, we can illuminate any desired plane with a laser sheet from the hub to the tip of the blades. The interrogated planes can be parallel or normal to the axis of the pump. The corner window also provides us with an optical access to the interior of the rotor and the stator, which is essential for future, 3-D, HPIV measurements.

Test setup No. 2 was constructed with ONR funding, and its primary objective has been to study the stability of swirling flows. In test setup No. 2 the first stage (rotor and stator) is identical to that of setup No. 1. However, the second stage consists of a stator followed by a rotor. A honeycomb occupies the entire gap between the two stator-rows. The purpose of this honeycomb is to reduce the effect of large-scale turbulence generated by the first stage, and to align the flow in the axial direction, consistent with the orientation of the first stator. This arrangement enables us to study the structure and evolution of the rotor wake with reduced disturbances from the first stage, and allows us to follow the rotor wake over a large distance. We have used both setups for examining the structure of turbulence in turbomachines. Due to the presence of a honeycomb, we also use the data of setup No. 2 to examine the structure of the rotor near wake and boundary layer due to the effect of an inlet guide vane at high magnification.

3.2 PIV Measurements:

The window that covers the entire second stage (Figure 3), and an additional transparent insert (not shown) contains a probe with the laser-sheet optics. We can illuminate any desired plane with a laser sheet from the hub to the tip of the blades, including the tip-gap. The light source is an Nd-YAG laser whose beam is expanded to a 1 mm thick light sheet. The flow is seeded using 20% silver coated, hollow glass, spheres, with a mean diameter of 13μm), the images are recorded using a single 2048×2048 pixels^2, Kodak Megaplus ES4.0, "cross-correlation" digital camera. A control system synchronizes between the PIV system and the signal of a shaft encoder. At least 100 instantaneous realizations are recorded and analyzed for each phase and

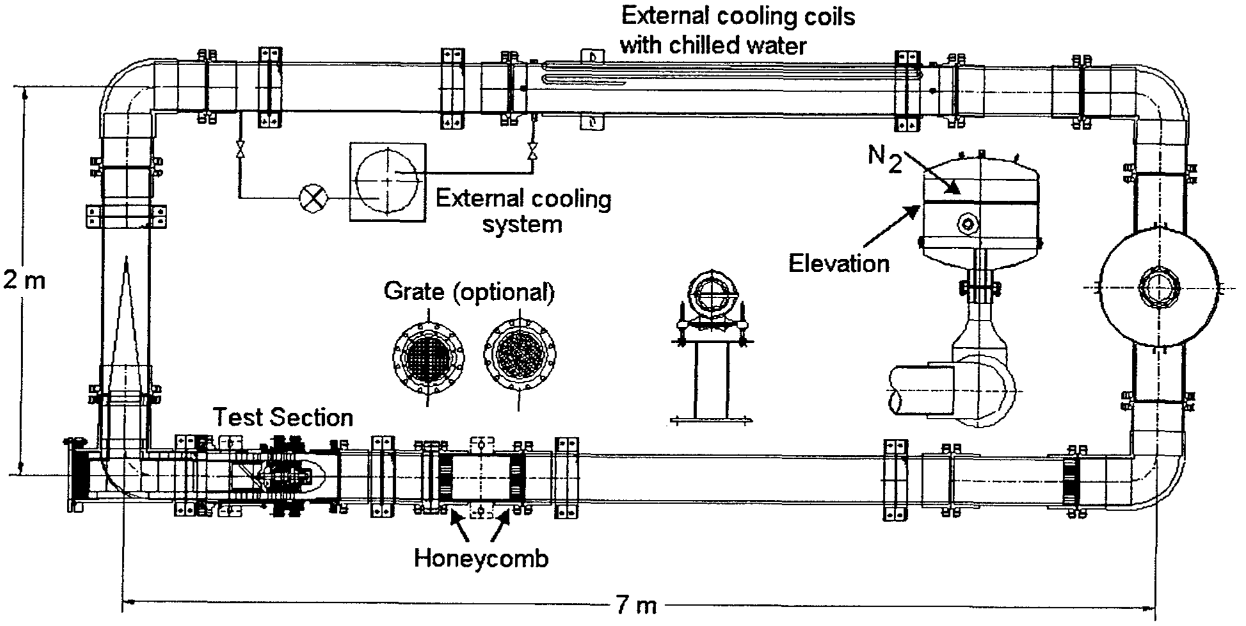

Figure 1: The Index matched axial turbomachine test facility at JHU.

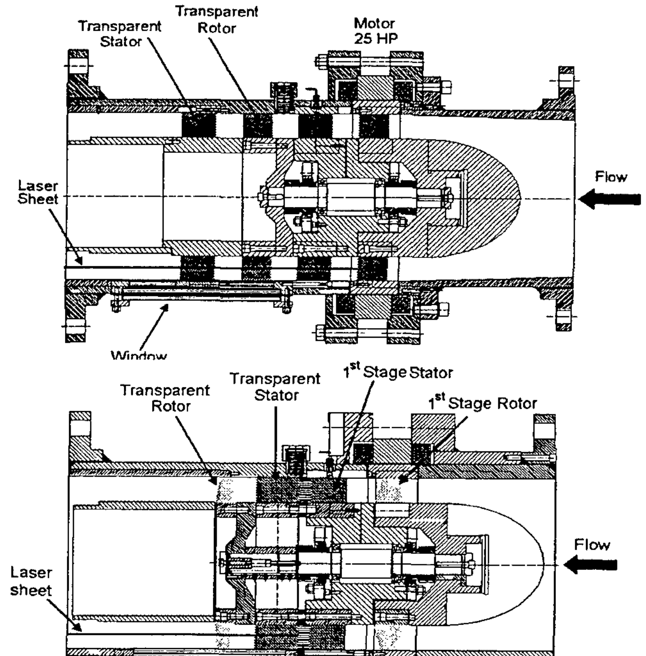

Figure 2. The axial turbomachine test setup No. 1 (top), and test setup No. 2. (bottom).

Table 1

	Test Setup	
	No. 1	No. 2
No. of stages	2	
No. of rotor blades	12	
No. of stator blades	17	
Hub-to-tip ratio	0.708	
R2-S2 axial gap/Rotor axial chord	1.92	1.41
S1-R2 axial gap/Rotor axial chord	1.95	N/A
Rotor pitch-to-chord ratio (mid-span)	1.34	1.34
Stator pitch-to-chord ratio (mid-span)	0.66	0.97
Rotor chord (mm)	50	50
Stator chord (mm)	73.2	50
Rotor and Stator span (mm)	44.5	44.5

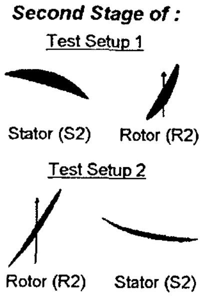

location to obtain the phase-averaged mean properties. To obtain converged turbulence statistics, it is necessary to record and analyze 1000 images.

For most of the data the sample area is 50x50 mm^2, and each velocity distribution consists of 64x64 vectors. Five data sets at different axial locations are needed to cover the entire 2nd stage. In order to characterize the turbulence in the near wake, and the flow structure within the boundary layer, during some of the measurements we increase the magnification to a sample area of 15x15 mm, and use interrogation windows of 32x32 pixels. With 50% overlap between windows, the resulting velocity distributions contain 128x128 vectors, with vector spacing of 120mm. Image enhancement and cross-correlation analysis are performed using in-house developed software (Roth et al. 1999; Roth and Katz, 2001). Some of the procedures have been modified to accommodate specific issues associated with the present data. Details are discussed in Uzol et al., 2002a). A conservative estimate for the displacement uncertainty is 0.3 pixels, provided the window contains at least 5-10 particles (Roth et al. 1999; Roth and Katz, 2001). For a typical displacement of 20 pixels, the uncertainty in instantaneous velocity is ~1.5%. Slip due to the difference between the specific gravity of the particle (1.6) and that of the fluid (1.8) causes an error of less than 0.2% (Sridhar & Katz, 1995).

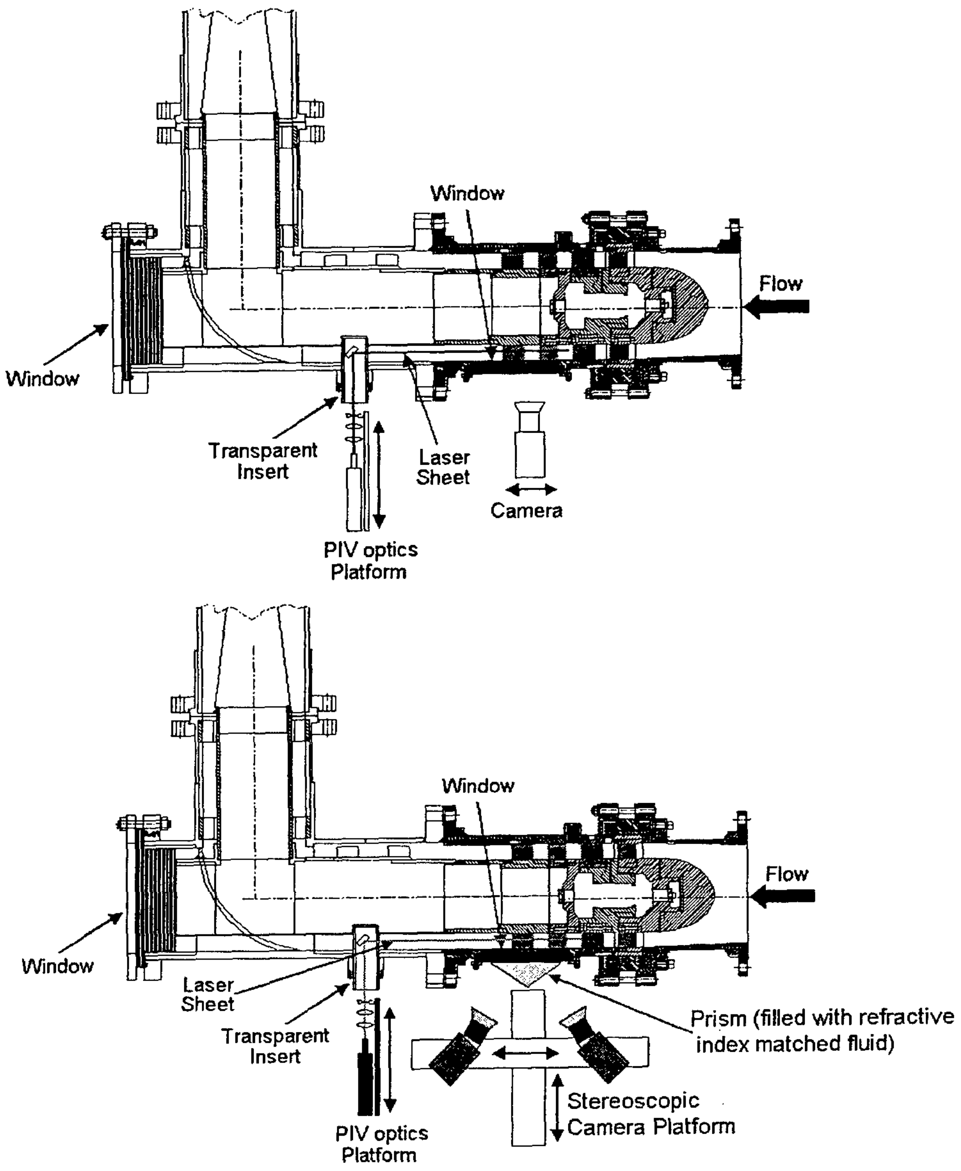

Figure 3: Optical setup for the 2-D PIV (top) and Stereo-PIV (bottom) measurements.

Stereoscopic PIV measurements require two digital cameras. The lenses are rotated to obtain a 30° viewing angle with respect to the access window (Figure 3, bottom). The CCDs are further rotated by another 14° to satisfy the Scheimpflug condition, i.e. to obtain a focused (but distorted) image of the illuminated plane. The region of overlap between the left and right cameras currently gives us a viewing area of 33.6 x 29.05 mm^2. In order to minimize the optical distortions that would occur at the liquid - air interface, we attach a prism containing a refractive index matched fluid to the access window. The prism windows are aligned with the lenses, and the prism location can behhh shifted to observe any parts of the sample area. During analysis each image is analyzed separately. Matching the data while correcting for the distortions, and subsequent calculations of the three velocity components from the two-dimensional vector maps are performed using Flow Manager 3D PIV software acquired from Dantec Inc. This software has been integrated into our in-house developed PIV analysis tools.

4. Results

In this Section we provide a brief summary on our progress in the AFOSR sponsored program. Within the three years duration of the present project, we have acquired, processed, analyzed and investigated about 30,000 PIV image pairs over a wide range of flow conditions, location and phases. The results have been used for characterizing the phase-averaged and average passage flow, the turbulence (and related parameters), the distributions of deterministic stresses and related parameters. It would be impossible to discuss all the results in a single report. Thus, we have chosen several examples illustrating the type of insight gained, and then summarize the findings and conclusions. Further details can be found in the five journal papers, four published and one still under review (Chow et al., 2002a, 2003a; Uzol et al., 2002a, b, 2003a), and ten conference papers (Chow et al., 2002b, c, 2003b, c; Uzol et al., 2001, 2002c, 2003b, 2004a, b; Soranna et al., 2004) that we have published/presented over the past two years. Sample velocity, vorticity and turbulent kinetic energy, along with estimates of dissipation rates are presented in Sections 4.1 and 4.5, the latter at a higher resolution. The average-passage mean flow and turbulence parameters, distributions of deterministic stresses, and the production and dissipation of deterministic kinetic energy are discussed in Sections 4.2 – 4.4. Issues related to distribution of SGS stresses and energy flux across scales are discussed in Section 4.6.

4.1 Phase-Averaged Mean Flow and Turbulence, 2-D data, Setup No. 1.

To study the dynamics of deterministic stresses using setup No. 1, the measurement domain covered the entire 2nd stage. Data have been obtained for 10 rotor phases, every three degrees of blade orientation, covering an entire rotor blade passage of 30°. In this section we provide data on three spanwise planes (containing the streamwise and lateral velocity components), which are located at 3%, 50% and 90% of the rotor span. Using the instantaneous measurements, the phase-averaged parameters are calculated from

$$
\begin{aligned}
\bar{u}_i(x,y,\phi) &= (1/N)\sum\nolimits_{k=1,n}(u_i)_k \\
\overline{u_i' u_j'}(x,y,\phi) &= (1/N)\sum\nolimits_{k=1,n}[(u_i)_k-\bar{u}_i][(u_j)_k-\bar{u}_j] \\
k &= (3/4)\overline{u_i' u_i'}
\end{aligned}
\tag{1}
$$

where N=100 (or 1000) is the number of instantaneous vector maps for each phase, x and y are the axial and almost circumferential (the light sheet is flat) coordinates, respectively, and ϕ is the phase angle. The subscripts i and j take values of 1 and 2, representing the axial and lateral velocity components, respectively. The 3/4 coefficient of k, the "turbulent kinetic energy", is selected to account for the contribution of the out of plane velocity component, assuming that it is an average of the available measured components (proposed 3-D measurements will address this issue). The phase-averaged vorticity is calculated using, $\bar{\omega}_z = \partial\bar{v}/\partial x - \partial\bar{u}/\partial y$.

As an example, in this Section we will compare the phase-averaged flow and turbulence in three planes, near the tip (90% span), near the hub (3% span) and at mid span (50%), all for setup No. 1. Figure 4 shows phase-averaged distributions of velocity magnitude and turbulent kinetic

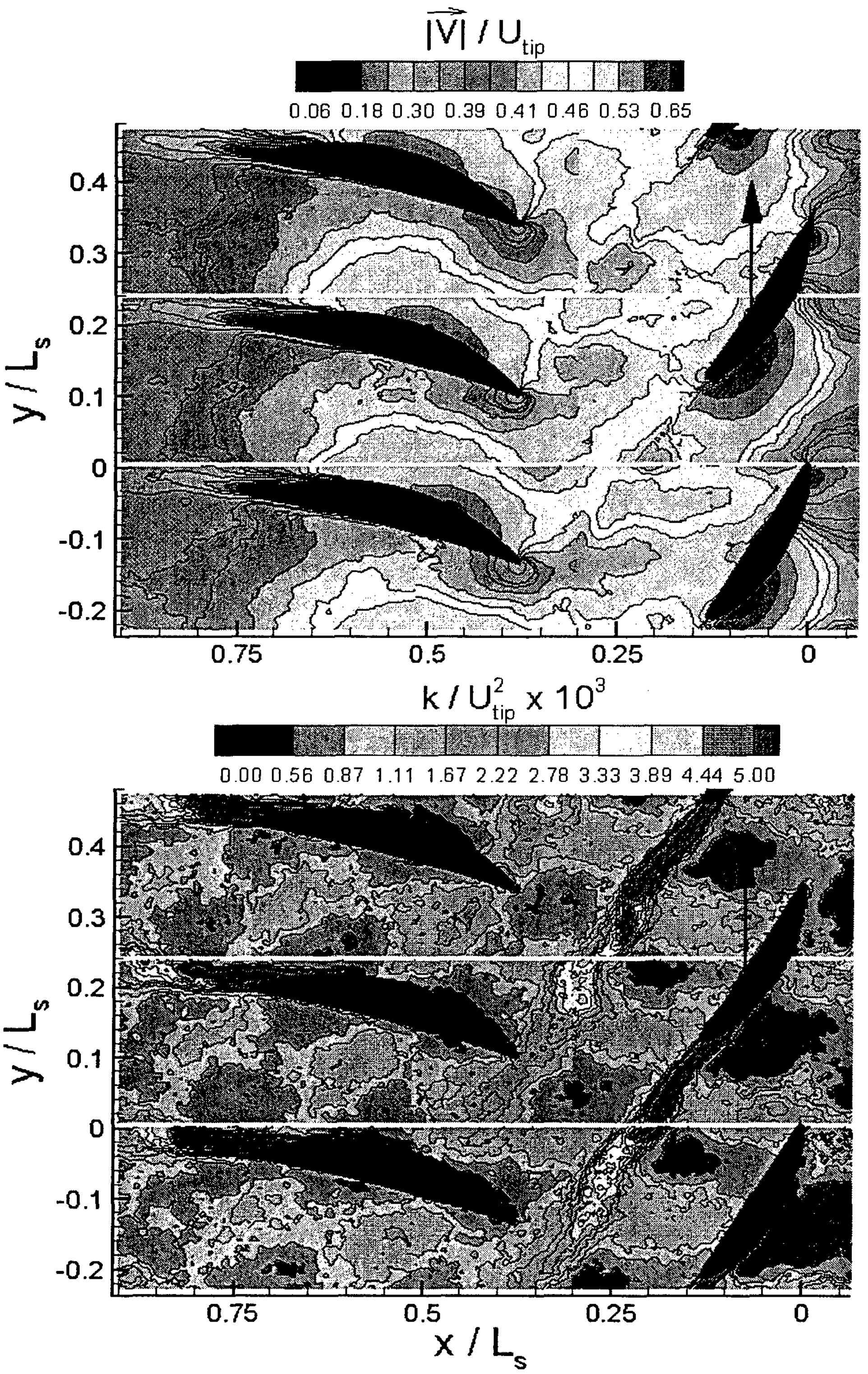

Figure 4: Matched three sets of phase averaged absolute velocity magnitude (top); and turbulent kinetic energy (bottom) at *mid span*, in the 2nd stage, setup no. 1.

energy at mid span at three different phases, matched to create a perception of a cascade. Figure 5 compares the phase-averaged distributions of axial velocity ($\bar{u}$), lateral velocity ($\bar{v}$), absolute velocity magnitude ($|\bar{V}|$), relative velocity magnitude ($|\bar{V}|_{rel}$), turbulent kinetic energy (k) and phase-averaged vorticity ($\bar{\omega}$) in the three planes, for one of the ten measured phases, t/T=0.0 (T is the rotor blade passing period). Figure 6 presents the vorticity distribution at a different phase (t/T=0.7) in order to highlight certain phenomena.

Figure 4 depicts a complex flow field, which is composed of a lattice of chopped-off rotor and stator wake segments. The wakes of the 1st stage stator blades arriving from the right side (the high turbulent kinetic energy regions, TKE, on the right hand side of each phase) are broken to segments by the (visible) 2nd stage rotor blades. The rotor also cuts through the wake of the 1st stage rotor, whose signature appears on the right side as inclined (diagonal) region with elevated TKE between the stator wakes. The combined effect of the 1st stage rotor and stator cause 10°-12° variations of inlet flow angle to the 2nd stage rotor, resulting in substantial (13%) variations in the work input (performance) of the rotor. The 2nd stage rotor wake is also chopped when it arrives to the 2nd stator. Traces of the 1st stage stator wakes can be identified all the way to the exit of the second (visible) stator as almost horizontal layers of elevated turbulence in the regions between the inclined rotor wake segments. Due to differences in velocity on the two sides of the rotor blades, the 1st stage stator wake becomes discontinuous across the rotor blade, and later across the rotor wake. As discussed in Section 4.3, these "discontinuities" shear and kink the rotor wake, creating a series of turbulent hot spots along the wakes.

Flow in the Tip Region: The flow field in the tip region (90% span) is dominated by the presence of the tip vortex. The vicinity of the tip vortex is characterized by low relative velocity magnitude (Figure 5d), high turbulent kinetic energy (Figure 5e), high lateral velocity (Figure 5b), and in part, wake-like distribution of vorticity (streaks of opposite signs on opposite sides of the wake, Figure 5f). The turbulent kinetic energy levels as well as the phase-averaged axial and lateral velocity non-uniformities in the flow field are substantially higher than those at mid-span. The tip vortex starts dissecting the 90% plane to the right (suction side) of the trailing edge of the blade that generates it (e.g. Figure 6). The large structures on the pressure side of the blade, which occupy most of the rotor blade passage, are generated by the previous blades. In Figure 5f one can see two such systems, the first near the pressure side of the blade, and the second in the rotor-stator gap. The "blobs" with high positive vorticity appear in regions where the tip vortex dissect the 90% plane, as can be deduced from the sharp gradients in horizontal and lateral velocity gradients (Figures 2a, b). Due to the vortex-induced velocity, $\bar{u}$ diminishes above the vortex center, and $\bar{v}$ decreases sharply to the right of the center. Recent measurements (Uzol et al., 2004a,b) have shown that these blobs develop as a result of vortex bursting that occurs as the tip vortex passes by the pressure side of the blade.

The tip vortex center is also characterized by high turbulence level. The tip vortex impinges on the pressure side of the following rotor blade and then interacts with the wake of that blade. The impingement is evident in Figure 5f at (x/Ls=0.12, y/Ls=0.04), as the concentrated positive vorticity region comes into contact with the blade. At t/T=0.7 (Figure 6) this very same region can be seen interacting with the wake of the rotor blade at (0.2, 0.16). During this interaction the rotor wake (of the subsequent blade) is split, and part of it is entrained by the tip vortex (of the previous blade). The split rotor wake segments merge with the tip vortex in the gap between the rotor and the stator (Figure 5f), and the resulting complex structure is transported through the stator passages. Thus, the positive and negative vorticity regions within the stator passage in Figure 5f are, in fact, combined tip vortex and (subsequent) rotor wake. It is not possible to

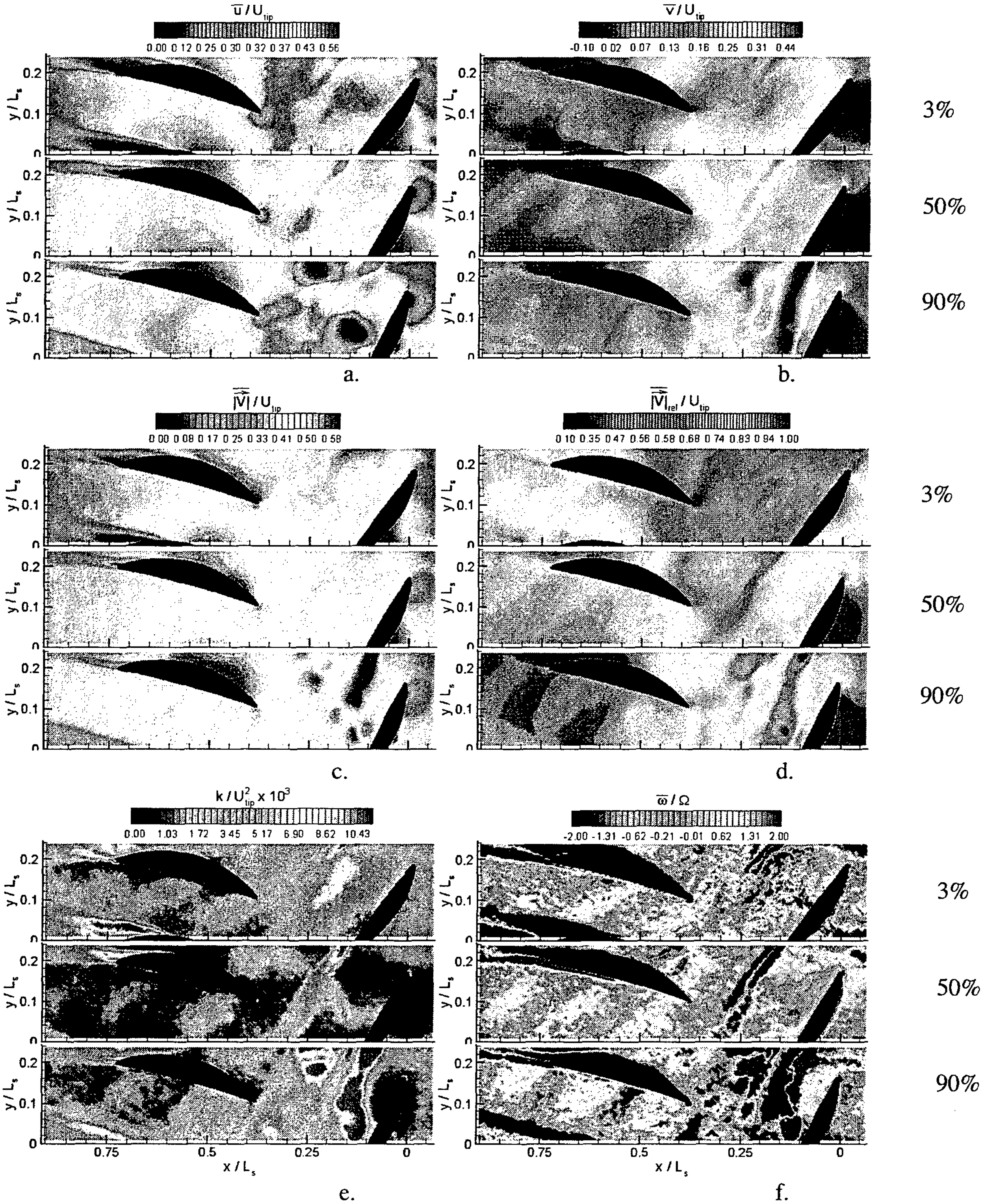

Figure 5. Phase-averaged distributions for t/T=0.0 of: (a) axial velocity; (b) lateral velocity; (c) absolute velocity magnitude; (d) relative velocity magnitude; (e) turbulent kinetic energy (k); and (f) vorticity at three spanwise planes (indicated as percentage of the span). U_{tip} = 8 m/s is the blade tip velocity at 500 rpm, L_S = 203 mm is the stage length and x=0 is the rotor leading edge. Ω=52.36 rad/s (500 rpm).

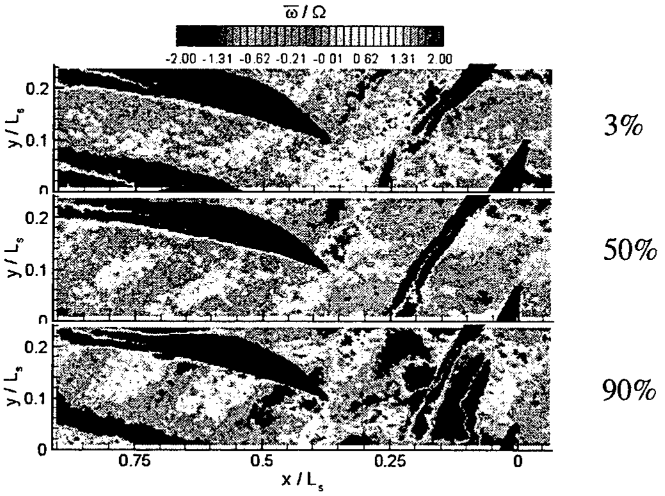

Figure 6. Sample phase-averaged vorticity distributions at three spanwise locations, at t/T=0.7.

distinguish the individual rotor wakes and the tip vortices in the stator passage once they merge together (unless one performs 3-D velocity measurements).

Upstream of (x<0) and within the rotor passage one can identify the wakes generated by the first stage. At the 50% plane (Figure 5f), one can see the lower half of a 1st stage stator wake with positive vorticity at (-0.05, 0.2), and the upper half of the following wake with negative vorticity at (-0.05, 0), as discussed in Uzol et al. (2002b, 2003a). The phase-dependent oscillations of the 1st stage stator wakes in the tip region are substantial compared to the mid-span, even upstream of the second stage rotor, as is evident by comparing the corresponding vorticity plots in Figures 5 and Figure 6. At mid-span the wakes do not change significantly, whereas at the tip the incoming stator wake is straight at t/T=0.0, and significantly distorted at t/T=0.7, most likely due to the flow field induced by the tip vortex. These periodic fluctuations of the 1st stage stator wakes become clearly evident when all measured rotor phases are examined as a sequence.

The first stage rotor blade row does not generate a tip vortex since it is banded by an external ring containing the permanent magnets of the rim-driven motor, and there is no tip gap. The wakes of the 1st stage rotor generates inclined vorticity layers with alternating signs (Uzol, 2002b). In Figure 5f (50%), the 2nd stage rotor blade dissects such an inclined wake, creating a layer of negative vorticity on the pressure side of the blade, and positive vorticity on the suction side. Thus, the rotor is engulfed by the 1st stage rotor wake. Due to spanwise variations in velocity, there are phase differences between the 1st stage rotor wake at mid span and in the tip region (90%). Consequently, in the tip regions the 1st stage rotor wake is located upstream of the blade. As a result, the inclined vorticity layers appear to have opposite signs, e.g. there is a positive vorticity layer on the pressure side of the blade in the tip region and a negative vorticity at mid span. The phase lag is also evident in Figure 6, before the blade interacts with the inclined wakes. At mid span the blade is aligned with the positive vorticity layer with the negative layer slightly downstream, and the rotor blade is about to slice through this wake. It the tip region, the 1st stage rotor wake is located upstream of the rotor blade. There are several possible reasons for delay, such as the effects of the boundary layer on the casing, both within the 1st stage stator passage and in the gap between stages.

Although the flow field in the tip region is quite complicated, the interaction of the incoming 1st stage stator wakes with the rotor blade and the tip vortex can still be depicted. The upstream stator wakes get chopped off by the rotor blades and then merge with the tip vortex. At t/T=0.0 (Figures 5e and f at 90%), the rotor blade is about to cut through the stator wake. At this instant this stator wake intersects with the tip vortex of the previous rotor blade at (0.09, 0.2). As the wake gets chopped off, the wake segment and the tip vortex merge along the pressure side of the rotor blade, generating concentrated positive vorticity regions, identifiable, for example, in Figure 6 at (0.27,0.06), (0.15,0.24), and in Figure 5f at (0.32,0.12). These high vorticity "blobs" enter the second stage stator passage along the suction side of the stator blade, and eventually become difficult to distinguish from the inclined structures generated by the tip vortices and entrained rotor wakes. These complex interactions near the tip create much wider, inclined patches of high vorticity in the tip region, as compared to the mid-span. Note that these processes are easier to recognize as one examines all the ten phases in sequence, and are virtually impossible to follow from the two samples presented here. However, since the flow in the tip region is three dimensional, one still has to guess/infer the structure of the out of plane velocity component in order to understand the flow structure. This problem can be resoled by performing three dimensional velocity measurements. Stereo PIV in closely spaced planes in the tip region have been performed recently, are already available in Uzol et al. (2004a, b).

In comparing the vorticity distributions at mid span to the tip region (Figure 5f), one can also notice that the wake of the previous blade is located further downstream compared to the structures in the tip region. Furthermore, the angle between the wake and the streamwise direction at mid-span is lower than the main orientation of structures in the tip region. These differences are caused by the lower axial velocity (presumable due to the casing boundary layer), and higher lateral velocities just downstream of the rotor blade in the tip region. As the tip vortex is transported in the rotor-stator gap, its advection angle is initially very steep, about 60° at $x/Ls<0.2$. However, as the tip vortex gets closer to the stator row, its advection angle decreases to about 40°, at $x/Ls>0.25$. The orientation of structures in the tip region remains higher than that at mid span throughout the entire stator passage.

The vorticity contours at the 90% span in Figure 5f also reveal a wake-like zone just above the 2nd stage stator wake. The positive vorticity layer can be seen above the stator wake at (0.7, 0.22), starting at mid-chord, and the negative layer (associated with a previous blade) can be seen on the bottom left side of the plot, along with parts of the positive vorticity layer at the (bottom left) corner. This phenomenon is most likely caused by some tip leakage flow at the stator blade tip. Although the stator blade is designed to come into contact with the window, the measurements indicate that there is some leakage. This leakage flow reduces the effective flow area at the exit from the stator, compared to the mid-span (see distributions of u, Figure 5a). This phenomenon occurs only in the three stator blades facing the window (and will be solved by sealing the gap in the future). The other blades of this stator, and all the blades of the 1st stage stator are banded by an external rings, which are manufactured with the blades as one unit.

To recapitulate, at mid span, the spatial non-uniformities in velocity are associated with wake-blade and wake-wake interactions (Uzol et al. 2002b, 2003a). In the tip region, there are numerous additional interactions involving the upstream wakes, the rotor blade wake and, most importantly, the tip vortex. The resulting non-uniformities and phase-dependent variations in the flow structure in the tip region are much higher than those at the mid-span. For example, the axial velocities in Figure 5a vary from very low (even negative) values at (0.15, 0.06) and (0.23, 0.23), just above the points of intersection between the tip vortices and the 90% plane, to very high values just below the tip vortex intersections. The non-uniformities in the lateral velocity are also much higher than at mid-span. Clearly, the largest spatial, phase-dependent variations are associated with the presence of the tip vortex. As the tip vortex is convected towards the stator passage, these phase-averaged non-uniformities sweep through the flow field, creating high phase-dependent velocity fluctuations. Thus, one should expect to find significantly higher levels of deterministic stresses in the tip region, as will be demonstrated in the next section.

Flow in The Hub Region (3% span): The flow field near the hub region is dominated by interactions between the rotor and stator wakes with the rotating and stationary hub boundary layers (The rotating hub section is located at $-0.07<x/Ls<0.2$). These interactions are the main causes of the phase-dependent unsteadiness and deterministic axial and lateral velocity fluctuations. Unlike the other spanwise planes, near the hub high lateral velocity is induced both by the blades and by the rotating hub. The levels of phase-averaged velocity non-uniformities appear to be lower than those at mid-span or the tip. Conversely, in most hub regions the turbulence levels are substantially higher than the levels at mid-span (Figure 5e). The 3% plane has a wide region with elevated turbulent kinetic energy, especially within the rotor passage and the rotor-stator gap. Figure 5f shows that the same domain contains several narrow vorticity layers, some with alternating signs (details follow). Inspection of all the available phase-averaged data reveals that the wide turbulent region is generated mainly within the rotor passages, presumably due to the rotating hub boundary layer (and its interaction with upstream structures), and are then convected through the stator passages while merging with the upstream rotor and stator wakes.

Chopping off and shearing of the 1st stage stator wakes are also observed near the hub. At $t/T=0.0$ (Figure 5f.), the rotor blade is approaching the upper stator wake, while it has already sheared the lower stator wake, which intersects with the blade at (0.1, 0.1). Figure 6, shows an early stage of stator wake shearing. The dominant phenomenon consists of several inclined vorticity layers, some with alternating signs that dominate the rotor-stator gap. This trend seems to repeat itself on the other side of the short rotor-wake segment. Well-founded explanation for the formation of these structures requires further analysis, and 3-D measurements (being planned). It seems, however, that a major contributor to this phenomenon is the transition from non-rotating to a rotating hub at $x/L=-0.07$, and the subsequent transition to a non-rotating hub at $x/Ls=0.2$. Such transitions generate a variety of three dimensional flow structures on their own (e.g. Bouda et al., 2002), as well as stretch and re-align upstream wakes. The negative inclined vorticity layer to the right of the rotor wake (Figures 6 and 5f) exists already at the entrance to the rotating section, and may even be initially part of the 1st rotor wake. The layer turns slightly upward within the rotor passage, presumably by the rotating boundary layer, and is then turned downward while gaining strength (maybe due to stretching), in part by the rotor blade, and in part by the transition to a non-rotating boundary. It is also possible that the increased strength is affected by the hub vortices on the rotor blade.

The origin of the inclined structures with positive vorticity is not obvious. They may be a result of interaction of the 1st stage stator wake segment (on the pressure side) with the combination of a rotating boundary layer and the pressure gradients in the rotor pressure side. Note that the positive inclined streaks are less evident in Figure 6, shortly after the stator wake is chopped off by the rotor. The lateral velocity (Figure 5b) peaks at the interface between the negative and positive vorticity layers, and consequently, the relative velocity (Figure 5d) is minimal at the same location. The turbulent kinetic energy also peaks at this interface, giving it a wake-like structure, which migrates downstream, and overwhelms the rotor wake signature. In fact, the structures seen being advected in the stator passage are originated by this phenomenon, and not by the rotor wakes. Clearly, analysis/explanation of this phenomenon requires additional extensive efforts.

Unlike mid span, where the rotor wake can be identified for a large distance, even after being deformed by upstream wakes (Chow et al., 2002a, 2003a), in the hub region, the wake of the upper rotor blade (which is out of the field of view at this phase) becomes much less distinct already at only a short distance downstream of the wake. In Figure 5f, the rotor wake can be identified only between (0.15, 0.23) and (0.2,0.18). The same rotor wake segment, with a similar length, can also be seen in Figure 6 attached to the rotor. Breakup of this wake occurs due to non-uniformities in streamwise velocity associated with the 1st stage stator wake, as discussed (for mid span) by Chow et al. (2002a). The streamwise velocity is lower within the stator wakes and higher between them. When the rotor wake is exposed to these non-uniformities, it is sheared. At mid span the shearing generates kink with elevated turbulence levels (hot spots), whereas in the hub region the rotor wake becomes discontinuous, and the presence of other large structures makes is very difficult to identify the broken segments.

The elevated levels of lateral velocity in the rotor-stator gap in the hub region result in relatively high flow angles at the stator inlet. The average stator inlet flow angle at the hub is 47°, whereas it is only about 34° at mid-span (The stator inlet flow angle at the tip is also relatively high, about 47°, due to the effect of the tip vortex). The high inlet flow angle at the hub affects the suction side boundary layer of the stator blade, especially on the downstream side. As is evident from the distributions of axial velocity, velocity magnitude, turbulent kinetic energy and vorticity in Figure 5, the boundary layer on the downstream side is much thicker, than the corresponding layers in the other planes. Furthermore, expansion of the boundary layer starts much earlier near the hub, at about *x/Ls*=0.55, compared to *x/Ls*=0.64 and *x/Ls*=0.66 at the mid-span and the tip, respectively.

It is interesting to note that, although the average stator inlet flow angles are about the same at the tip and the hub, the suction side boundary layer starts to get thicker much later at the tip. This difference is most likely related to flows (and associated pressure gradients) induced by the tip vortex. Figure 7 compares the distributions of phase-averaged velocity magnitude along the suction side of the stator blade near for the hub, mid-span and tip regions, all at the same phase, t/T=0.7. The substantially higher momentum loss near the hub, especially at x/Ls>0.55, is evident. However, there is no reverse flow along the suction side of the upper stator blade in the 3% plane, namely there is no evidence of flow separation at this plane.

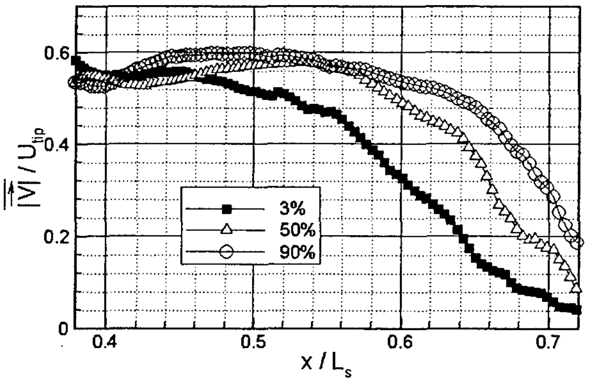

Figure 7. Absolute velocity magnitude distributions along the suction side of the stator blade for the 3%, 50% and 90% spanwise planes, all at t/T=0.7.

Although thickening of the boundary layer occurs on both stator blades that are within the field of view, there are slight differences between them. In fact, weak reverse flow develops along the suction side of the lower stator blade, starting from x/Ls=0.65. Thus, local boundary layer separation occurs on the lower blade, but does not occur on the upper blade at all phases. These circumferential differences are not caused by differences in flow fields. They are a result of using a flat 50x50 mm^2 measurement plane (laser sheet) that is perpendicular to surface of the upper blade (which is located at the center of the window). Consequently, the upper blade is dissected at the 3% plane, whereas the lower blade is dissected at the 15% plane. We suspect that the 3% plane is located closer to the wall, and possibly below the hub vortex, whereas at the 15% plane we dissect the hub vortex, leading to differences in velocity distributions. The radial differences in the points of dissecting the blades exists also in these planes, but their impact is largest near the hub, in part due to the smaller radius of curvature, and in part due to large spanwise variations in flow structure near the hub. The deviations at mid-span and the tip are 10% (50% and 58% on the upper and lower blades, respectively) and 8% (90% and 98%), respectively. Consequently, the lower blade seems to be affected more by the leakage at the tip of the stator blade.

4.2 Average-passage flow fields, turbulence, and deterministic stresses

The measured phase averaged flow fields at ten different rotor phases, every 3° of rotor orientation, which cover the entire rotor passage, enable us to calculate the average-passage flow fields and distributions of deterministic stresses. Recall that each of the present phase-averaged flow fields is an ensemble average of 100 instantaneous realizations. Thus, the "average-passage" flow fields presented in this section are obtained by "time averaging" of the "ensemble averaged" parameters. We do not account for passage-to-passage variations. The average-passage velocity, u_i^s, i=1,2, deterministic stress, $\widetilde{u_i"u_j"}$, and deterministic kinetic energy, k_{det}, are calculated from

$$\tilde{u}_i^S(x,y)=\frac{1}{T^R}\int^{T^R}\bar{u}_i^S(x,y,t)dt\approx\frac{1}{M^R}\sum_{m=1}^{M^R}\bar{u}_i^S(x,y,\phi_{R,m}) \qquad (2)$$

$$\widetilde{u_i''u_j''}^S(x,y)=\frac{1}{M^R}\sum_{m=1}^{M^R}\left[\bar{u}_i^S(x,y,\phi_{R,m})-\tilde{u}_i^S(x,y)\right]\left[\bar{u}_j^S(x,y,\phi_{R,m})-\tilde{u}_j^S(x,y)\right] \qquad k_{\text{det}}=0.5\,\widetilde{u_i"u_i"}$$

where M is the number of phase averaged realizations, "~" denotes an average-passage quantity, " " " represents the deterministic fluctuation (differences between averaged passage and phase-averaged value) and "s" indicates a stator frame of reference. Other average-passage parameters are calculated using the same procedure. For example, the averaged passage turbulent kinetic energy is calculated by replacing $\tilde{u}_i^s$ with $\tilde{k}$. Since the measurements provide a finite number of phases, the blades do not cover each point at the same frequency. As a result, the average-passage data becomes patchy, especially within the passages. To provide a smooth transition, in the initial data sets we constructed additional interpolated fields every 0.75° of rotor orientation. The process was based on linear interpolation of the experimental data in points that are circumferentially shifted according to their phase (Uzol et al., 2002b, 2003a). In this report we focus on spanwise variations of the passage-averaged flow parameters in the stator frame of reference. Uzol et al. (2002b) presents results at mid span in both the rotor and stator reference frames.

Figure 8 shows the distributions of average-passage velocity magnitude, vorticity, turbulent kinetic energy and Reynolds shear stress, as well as the distributions of deterministic kinetic

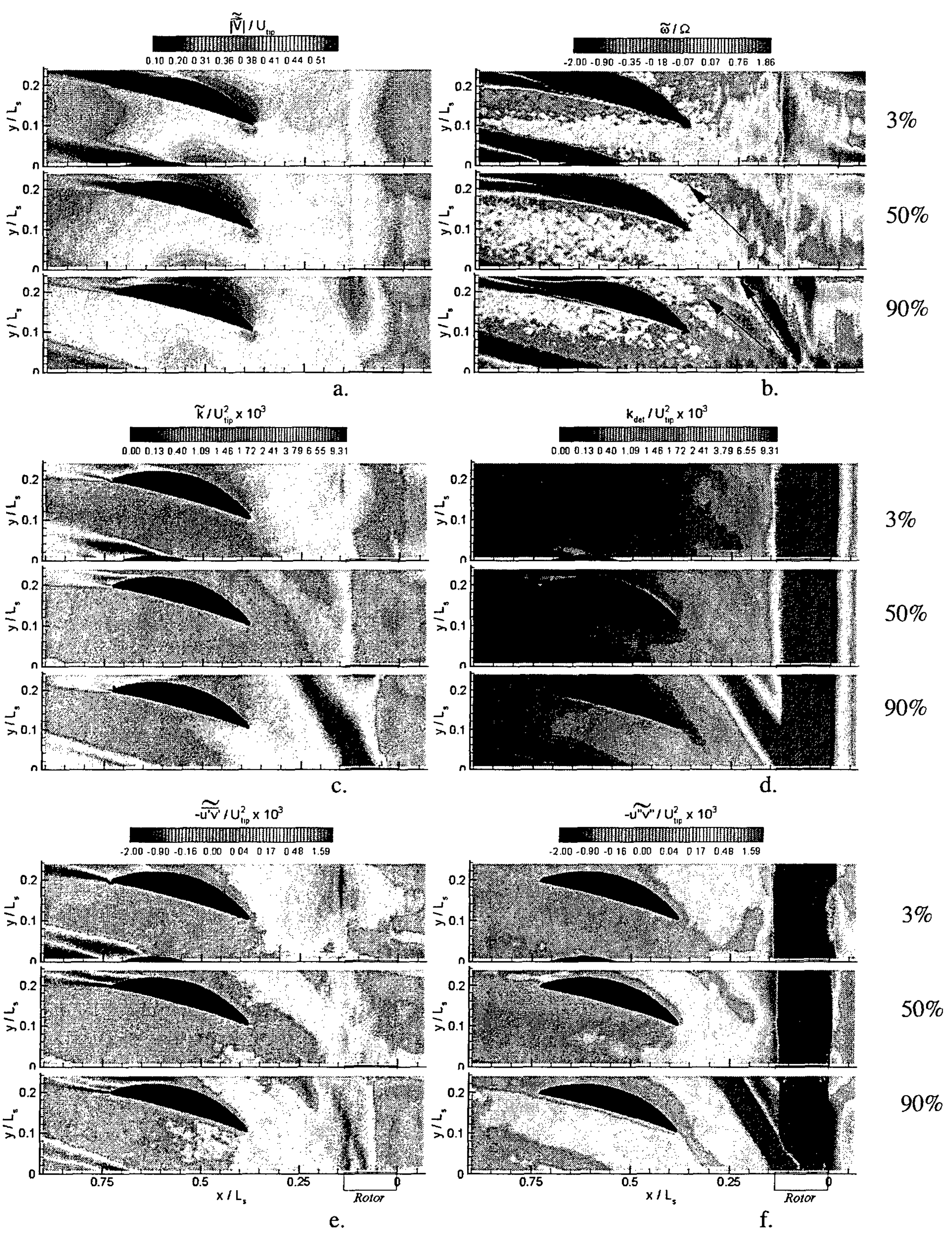

Figure 8. Average-passage (a) velocity magnitude (b) vorticity (c) turbulent kinetic energy (e) Reynolds shear stress and (d) deterministic kinetic energy (f) deterministic shear stress contours at 3, 50 and 90% spanwise locations in the stator frame of reference. In the vorticity plots, the arrow at 50% span and the arrow on the left at 90% span indicate upstream stator wake transport directions. The arrow on the right at 90% span vorticity plot shows the tip vortex transport direction.

energy and deterministic shear stress. As before, we compare the distributions in the 3%, 50% and 90% spanwise planes. Several observations can readily be made:

a. The highest deterministic kinetic energy levels develop immediately downstream of the rotor (except for the rotor passage). The decay process starts within the rotor-stator gap and extends into the stator passages. There are substantial circumferential non-uniformities in the distribution of k_{det} in any plane, but the most striking variations occur in the tip region.

b. Average-passage flow in the tip region: At 90% span, the average-passage vorticity contours (Figure 8b) reveal two separate, inclined, wake-like vorticity distributions in the rotor-stator gap, both of which are marked by arrows. The structure with a steeper angle, about 55°, is associated with the trajectory and advection of the tip vortex. The arrow is aligned with the direction of tip vortex transport. This region is also characterized by a very low axial and high lateral velocity components (not shown), very high average-passage turbulent kinetic energy (Figure 8c) alternating signs of average-passage Reynolds shear stress that coincide with the regions with alternating vorticity signs (Figures 8e), and extremely high deterministic kinetic energy (Figure 5d). The wake-like layers of alternating vorticity signs with a shallower angle, about 39°, are associated with advection of the chopped wake segments generated by the 1st stage stator blade. This association was concluded from observations of phase-dependant distributions of vorticity. This wake transport direction also coincides with the low velocity magnitude region in Figure 8a that extends diagonally from (0.15, 0.0) to (0.22, 0.1). As is evident, transport of the stator wake segments and advection of the tip vortex occur along different paths. Hence, they may even be transported through different passages in the stator blade row.

The transport direction of segments of the 1st stage stator wake at 50% span is also indicated by an arrow in the corresponding vorticity plot in Figure 8b. The advection angle in this plane, 38°, is very close to that at the tip, but the wake occupies a wider region compared to the tip region, as is evident from the wide positive and negative vorticity zones on either side of the arrow. Near the tip the stator wake segments are ingested in part by the tip vortex, reducing the domain directly affected by their advection.

c. At the hub, the wake transport direction is not as distinct as the clear trajectories at the mid-span or the tip regions. The complex flow structure generated by interaction of wakes with the rotating and stationary boundaries, as discussed before, are responsible for the reduced clarity. These interactions also contribute to the elevated levels of passage averaged turbulent kinetic energy in the rotor-stator gap (Figure 8c). One can still identify regions with predominantly positive and negative vorticity, but the rotor-stator gap does not contain distinct wake-like layers with alternating signs. However, the corresponding distribution of deterministic kinetic energy within the gap (Figure 8d) still shows a region with elevated levels that extends diagonally from (0.2,0.1) to (0.35,0.2), and continues within the stator passage. The elevated level of k_{det}, is associated with unsteadiness in the transport of the complex near-hub structures demonstrated in Figures 5 and 8.

d. Average-passage flow field around the stator: The previously discussed spanwise variation in the thickness of the boundary layer on the suction side of the stator, as well as the resulting effects on the wake thickness and effective exit flow area are clearly evident from the average-passage velocity and vorticity distributions (Figures 8a and b). Substantial non-uniformities that exist in the average-passage velocity magnitude in the gap extend into the stator passage. They are caused by the complex wake-blade, wake-wake, wake-tip vortex and wake-hub interactions discussed in the previous section (and in more detail in Uzol et al., 2002b, 2003a). The average-passage velocity fields also reveal that the point of maximum velocity on the suction side of the stator shift downstream as we go from the hub to tip. This trend indicates that the stator blades are more front-loaded close to the hub and more aft loaded in the vicinity of the tip.

e. Distributions of deterministic kinetic energy: The highest deterministic kinetic energy levels develop immediately downstream of the rotor (except for the rotor passage). The decay process starts within the rotor-stator gap and extends into the stator passages. There are substantial circumferential non-uniformities in the distribution of k_{det} within the gap in any plane, but the most striking variations occur in the tip region. The highest levels of deterministic kinetic energy, and the only ones that exceed the turbulent kinetic energy, occur along the tip vortex and wake trajectories (mostly the tip vortex) in the 90% plane. The origin of these high k_{det} values can be identified in the phase-dependent, spatially non-uniform velocity distributions associated with transport of the tip vortex and its interaction with the wakes that it encounters. Along the tip vortex trajectory, the levels of k_{det} are more than one order of magnitude higher than the levels at the hub and mid-span, and are of the same order of magnitude as the turbulent kinetic energy (Figure 8c). From mid-span to tip, the turbulent kinetic energy increases by about 5 times, whereas the deterministic kinetic energy increases by more than an order of magnitude.

The high levels of k_{det} along the tip-vortex trajectory extend to the entrance and into the stator passage. Even within the passage they are still about 4 times higher than the levels at mid-span and hub regions. Note that within the shown passage, the region with elevated level of k_{det} is an extension of the transport direction of a tip vortex generated by the rotor blade located below the sample area. The deterministic kinetic energy decays within the stator passage. This decay may be a result of vortex breakup due to interaction with other structures, or it can also be caused by the vortex migrating out of the 90% plane, but we cannot provide a substantiated explanation for this trend using the present data. Measurements in neighboring planes, as well as 3-D measurements in an axial plane are needed to track the vortex trajectory. Outside the tip vortex transport direction within the gap and the stator passages, the turbulent kinetic energy levels are still 3-4 times higher than the deterministic kinetic energy.

f. Other Trends of the deterministic kinetic energy: In the rotor-stator gap the deterministic kinetic energy levels at mid-span are about 30% higher than the levels at the hub within the gap. This difference can be attributed to the more spatially uniform phase-averaged velocity distributions in the hub (Figures 5, 6). A region of elevated deterministic kinetic energy exists also in the hub region, along the edge of the separated region on the suction side of the bottom stator blade. This phenomenon is associated with phase-dependent fluctuations in the boundary of the separated region, caused by transport of structures through the stator passage. Elevated levels can be observed near the trailing edges of the upper stator blade and near wake at mid span. This pattern is associated with modulation of the flow in the aft region by advected rotor and upstream stator wake (Uzol et al., 2002b, 2003a).

In contrast to the distributions of k_{det}, the turbulent kinetic energy in the hub region is only 2-3 higher than the corresponding levels at mid-span, especially in the region with complex interaction of wakes with the (fixed and rotating) boundaries. Recall that the rotating section extends to x/Ls=0.2. Within the tip vortex region, the maximum turbulent kinetic energy is about 5 times than the levels at mid-span.

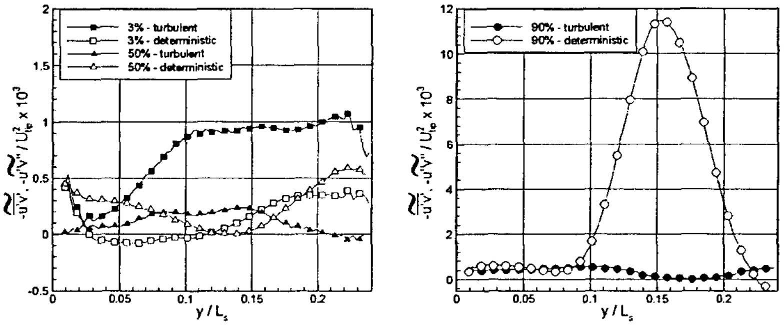

Figure 9. Deterministic and turbulent shear stresses at *x/Ls*=0.2 (in the rotor-stator gap) at the 3%, 50% (top) and 90% (bottom) spanwise planes. Solid symbols: Reynolds shear stresses; hollow Symbols: deterministic shear stresses. Note the differences in scales.

g. Distributions of deterministic shear stresses: The deterministic and (passage-averaged) turbulent shear stresses have comparable magnitudes, but different structures, in most areas, and in all spanwise locations. The only exceptions are the wakes of the stator blades where the turbulent stresses are much higher, and the tip vortex region, where the deterministic stresses are substantially higher. The trajectory of the tip vortex is characterized by concentrated layers with positive and negative deterministic and Reynolds stresses with opposite signs. However, the deterministic shear stresses are about an order of magnitude higher than the passage-averaged Reynolds stresses. Quantitative demonstration of the differences in magnitudes and trends between Reynolds and deterministic stresses along an arbitrarily selected line in the rotor-stator gap is presented in Figure 9. Other noted differences include higher turbulent shear stresses in the 3% plane and within the gap region. Conversely, at mid span the levels are close, but they have opposite signs. The negative and positive (deterministic and Reynolds) stress layers in the mid-span gap are associated with transport of the upstream stator wake and its interaction with the rotor wake. In the middle of the stator passage, the deterministic shear stress is higher than the turbulent stress at the tip, but the trend is reversed in the hub and the mid-span planes.

Along the suction side of the stator blade, there is a region with negative deterministic shear stress. This region is much wider at the tip, and it is narrowest at mid-span. As will be shown in the next section, this region is characterized by negative deterministic energy production, i.e. flux of energy from the deterministic kinetic energy to the averaged-passage kinetic energy. Before concluding, one should note that there are many additional phenomena that can be observed by careful examination of the distributions in Figure 8. We have only discussed those that have an impact on the dynamics of deterministic stresses.

4.3 Decay Rates Of Deterministic And Turbulent Kinetic Energies

Figures 10a and b show the variations of the normalized deterministic and turbulent kinetic energies along the stator mid-passage at the 3%, 50% and 90% span locations. Since all levels are normalized with their respective inlet values, these distributions actually show the corresponding decay patterns. The x-coordinate starts from x/Ls=0.38, i.e. at the plane of the stator leading edge. The y-coordinate is set to the mid-passage coordinate at every x. The stator trailing edge is located at x/Ls=0.73. Several observations can be made as follows:

The values k_{det} decrease gradually along the stator passage at all spanwise locations. At the exit of the stator blade row, 68%, 80% and 82% of the inlet deterministic kinetic energy is already dissipated at the tip, mid-span and the hub planes, respectively. The decay continues downstream of the stator, and at x/Ls=0.9, the levels are only about only 5.6%, 10% and 12.5% of the respective hub, mid-span and tip inlet values, i.e. there is a one order of magnitude decay in all cases. The decay rates vary between planes, most likely due to variations in the local dominant flow phenomena (as discussed before). For example, in the hub region, the decay rate of k_{det} (Figure 10a) is quite slow until x/Ls=0.5, and only about 30% of it is lost until that point. Just

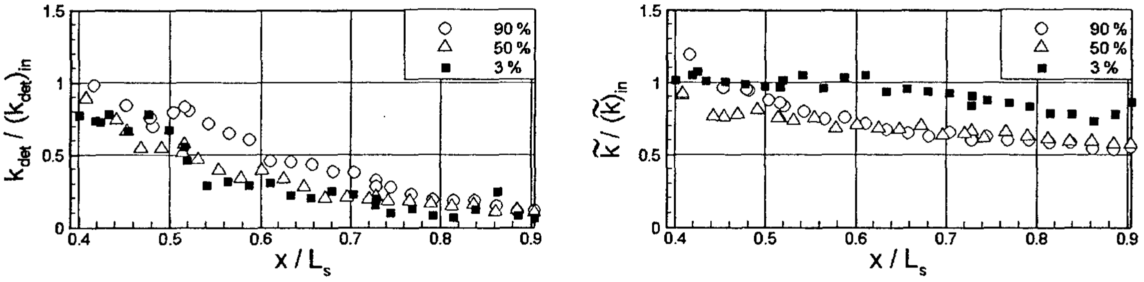

(a) (b)

Figure 10. Distributions of (a) deterministic (b) average-passage turbulent kinetic energy along the stator mid-passage at the 3%, 50% and 90% spanwise planes. The levels are normalized by the respective inlet values. The x-coordinate starts at the stator leading edge plane (x/Ls=0.38), and the stator trailing edge is located at *x/Ls*=0.73.

downstream of this point, there is a sudden drop to about 30% at x/Ls=0.54. In the tip region, the values remain flat up to x/Ls=0.52, and then decay at a faster pace.

Figure 10b demonstrates that the decay rates of the turbulent kinetic energy are much smaller than those of k_{det}. The decay rate at the tip and mid-span planes are very close to each other, and at the exit from the stage only about 40% of the turbulent kinetic energy is dissipated. At the hub, the turbulent kinetic energy decay rate is even slower, and it is only 20% lower by *x/Ls* =0.9. This lower decay rate is most likely associated with turbulence production in the hub boundary layer, which feeds turbulent kinetic energy into the 3% plane..

The fast decay of the deterministic kinetic energy within the stator, points to the fact that significant amount of "wake recovery" may occur along stator passage. The term wake recovery refers to reduction in dissipation rate (mixing loss) of a turbulent wake due to reduction in its velocity deficit, caused by straining within the stator passage. This process was first suggested by Smith (1966). Adamczyk (1996) showed, using a 2-D perturbation analysis, that the difference in the mixing loss is equal to the change in the flux of deterministic kinetic energy from inlet to the exit. Therefore, when the ratio of the exit to inlet deterministic kinetic energy fluxes is less than one, wake recovery process occurs, and the mixing loss of the upstream wake is reduced. In the present experiments, the ratios of exit to inlet deterministic kinetic energy flux are much less than one at all spanwise locations. Averaging the fluxes of deterministic kinetic energy at the inlet (leading edge) and the exit (trailing edge) of the stator passage, we obtain exit to inlet flux ratios of 29%, 17%, and 28% (i.e. reductions of 71%, 83% and 72%) for the hub, mid-span and tip planes, respectively. These trends are consistent with previous experimental results obtained by Van Zante et al. (2002) for NASA Stator37 at peak efficiency and 75% span, in which they reported a 71% reduction in the flux of deterministic kinetic energy.

4.4 deterministic kinetic energy budget

The momentum equations for the deterministic fluctuations, u_i'', are obtained by subtracting the average-passage RANS equations from the RANS equations. Then, a scalar product of u_j'' with the momentum equation for u_i'', and time averaging provides the transport equations for the deterministic stresses. The following deterministic kinetic energy transport equation is obtained as the trace of the equation of deterministic stresses:

$$\tilde{u}_k \frac{\partial}{\partial x_k}\left(\frac{1}{2}\tilde{u}_i\tilde{u}_i\right) = \widetilde{u''_i u''_k}\,\frac{\partial \tilde{u}_i}{\partial x_k} + \widetilde{\overline{u'_i u'_k}}\,\frac{\partial \tilde{u}_i}{\partial x_k} - \nu \frac{\partial \tilde{u}_i}{\partial x_k}\frac{\partial \tilde{u}_i}{\partial x_k} - \frac{\partial}{\partial x_k}\left[\tilde{u}_i\,\widetilde{u''_i u''_k} + \frac{1}{\rho}\tilde{p}\tilde{u}_i\delta_{ik} + \tilde{u}_i\,\widetilde{\overline{u'_i u'_k}} - \nu\frac{\partial}{\partial x_k}\left(\frac{1}{2}\tilde{u}_i\tilde{u}_i\right)\right] \qquad (3)$$

$$\tilde{u}_k \frac{\partial}{\partial x_k}\left(\frac{1}{2}\widetilde{u''_i u''_i}\right) = \underbrace{-\widetilde{u''_i u''_k}\,\frac{\partial \tilde{u}_i}{\partial x_k}}_{P_D} + \underbrace{\widetilde{\overline{u'_i u'_k}''\,\frac{\partial u''_i}{\partial x_k}}}_{D_T} - \nu\,\widetilde{\frac{\partial u''_i}{\partial x_k}\frac{\partial u''_i}{\partial x_k}} - \frac{\partial}{\partial x_k}\left[\frac{1}{2}\widetilde{u''_i u''_i u''_k} + \frac{1}{\rho}\widetilde{u''_i p''}\delta_{ik} + \widetilde{u''_i\,\overline{u'_i u'_k}''} - \nu\frac{\partial}{\partial x_k}\left(\frac{1}{2}\widetilde{u''_i u''_i}\right)\right] \qquad (4)$$

As before, "~" (tilde overbar) denotes time averaging over all phases (average-passage values) and straight overbar denotes ensemble averaging. Double prime, " '' ", refers to deterministic fluctuation and a single prime, " ' " is a turbulent fluctuation. The first three terms on the right hand side are source/sink terms. The first one (including the minus) is a production/dissipation term due to deterministic stresses and will be called "deterministic production (P_D)" in the following discussion. This term also appears in the transport equation of the average-passage kinetic energy with a reversed sign, and determines the energy transfer between the phase-averaged and average-passage flow fields. The second term is production/dissipation due to the deterministic fluctuations of turbulent (Reynolds) stresses and will be called "dissipation due to turbulence (D_T)". The reason for defining this term as dissipation (instead of production) will become evident in this section. The third term is the viscous dissipation associated with gradients of deterministic velocity fluctuations. The last four terms involve spatial transport of deterministic kinetic energy, but do not participate in production or dissipation.

The present experimental data enable us to determine *in-plane* distributions of all terms on the right hand side of Equation 3, except for the pressure-velocity correlation term. Of course, one has to keep in mind that out-of plane (3-D) effects may have a significant impact on the results, especially in the hub and tip regions. Nevertheless, as the following discussion shows, many interesting trends are revealed from the in-plane components. Distributions of the first two terms

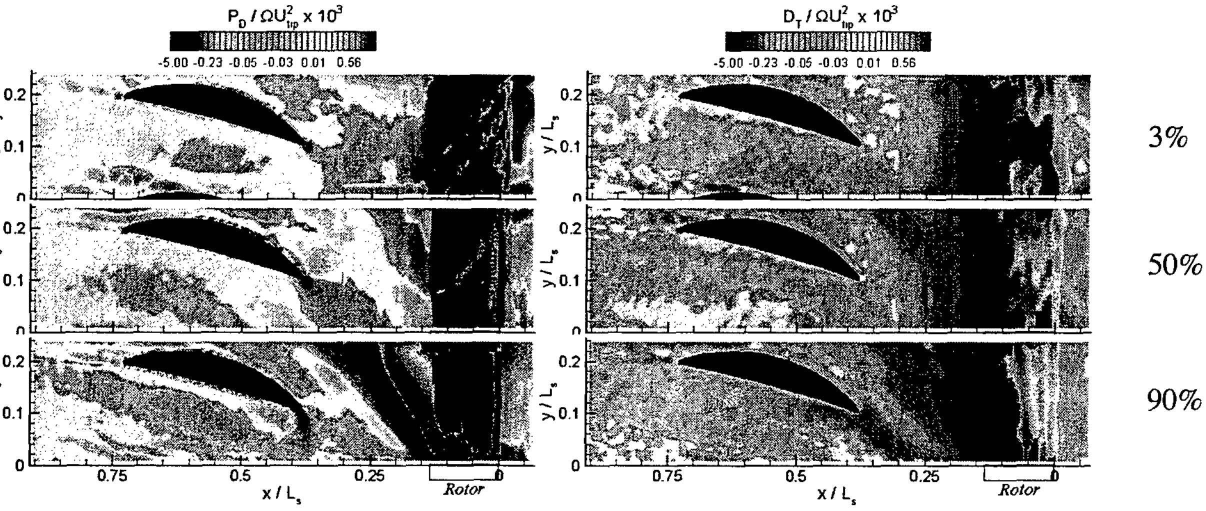

a. b.

Figure 11. Distribution of (a) deterministic production (P_D, term 1); (b) Dissipation due to turbulence (D_T, term 2) on the right hand side of the deterministic kinetic energy transport equation (Equation 3) at the 3%, 50% and 90% spanwise planes.

on the right hand side of the deterministic kinetic energy transport equation, i.e. deterministic production and dissipation due to turbulence are presented in Figure 11. Some observations can be summarized as follows:

a. P_D *and* D_T are the dominant source/sink terms in the Equation 3. The third, viscous dissipation term is 3 to 4 orders of magnitude smaller. There are regions in the flow field where either P_D or D_T are substantially larger than one another, sometimes by orders of magnitude, and in other regions they are of the same order.

b. As is evident from Figure 11a, there are distinct regions in the flow field with positive and negative deterministic production. Since this term is common to the average-passage and deterministic kinetic energy transport equations (with opposite signs), the results show that energy transfer between the phase-averaged and average-passage flow fields occurs in both direction. Adamczyk (1996) showed that the sign of the volume integral of P_D determines whether the wake mixing loss is reduced or increased by passing through a blade row. Negative volume-averaged deterministic production indicates reduction in mixing losses (associated with a decrease in deterministic kinetic energy). However, Adamczyk's analysis does not account for the effect of D_T on the evolution of the deterministic kinetic energy. Since D_T is mostly negative, the deterministic kinetic energy may decrease in spite of the fact that P_D is positive.

c. D_T *is negative almost everywhere*, and its magnitudes are particularly high downstream of the rotor, along the tip vortex trajectory (extending into the rotor-stator gap), and in parts of the wake transport direction at mid span. Hence, we refer to this term as the "dissipation due to turbulence". The loss of deterministic kinetic energy to turbulence should be accounted for, especially in these regions. At mid span, P_D is typically larger than D_T upstream of the stator passage, starting from x/Ls=0.3, and in the middle of the stator passage.

d. In the tip region, along the tip vortex transport direction, there are parallel layers with high values of P_D with opposite signs. Thus, in part of the tip vortex, energy is transferred from deterministic kinetic energy to passage-averaged energy. However, adding the first two terms in Equation 3 would still result in negative values, i.e. the deterministic kinetic energy decays in the tip region of the rotor-stator gap. One should also keep in mind that the flow in the tip region is highly three dimensional, and the missing out-of-plane terms may have a significant contribution to the overall balance.

e. Near the hub, in the rotor-stator gap, the deterministic production is predominantly negative, much more than at mid span. This trend is consistent with the higher passage-averaged velocity magnitude in the same region (Figure 8a), and the faster decay of deterministic kinetic energy near the hub (Figure 8d) compared to mid span.

f. There is also a wide negative deterministic production region upstream of the leading edge of the stator blade, and a narrower domain along the suction side of the stator boundary layer until about x/Ls=0.45. Further downstream, P_D becomes and remains positive through the trailing edge and the stator wake. A similar behavior occurs in the tip region, but the negative region is extended further downstream, ending at about x/Ls=0.5. This phenomenon does not occur at the hub and P_D is always positive along the suction side of the stator blade. High positive P_D values occupy substantial parts of the rotor-stator gap, especially the regions dominated by wake transport in the mid span and tip regions.

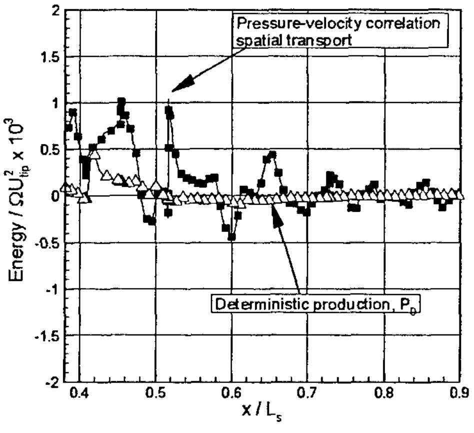

Figure 12. Distributions at mid-span of the deterministic production (P_D, term 1) and divergence of the deterministic pressure-velocity correlations (term 5) along the mid-passage of the stator.

g. *Spatial transport of deterministic* kinetic energy due to deterministic fluctuations, term 4 on the right hand side of Equation 3, and the transport term due to Reynolds stress fluctuations (term 6), are usually of the same order of magnitude as the deterministic production and dissipation due to turbulence terms. Although not presented here, it is observed that term 4 is a dominant production term around the rotor leading edge region. It is about one order of magnitude higher than deterministic production and about 3 to 4 orders of magnitude higher than the other terms. The deterministic production itself is also positive in this region.

Since all the *in-plane* terms of Equation 3 (including advection by the average passage velocity on the left-hand side) except the pressure-velocity correlation can be calculated, it is possible to estimate the pressure-velocity correlation term from a balance of the other terms. Since one expects the three-dimensional effect to be minimal at mid span, such an estimate is more likely to yield reasonable results at mid span. Thus, we perform the analysis using the mid-span data. Figure 12 compares the deterministic production term to the divergence of the pressure-velocity correlation term along the stator mid-passage. As is evident, the pressure-velocity correlation term is much larger than the deterministic production term, especially within the rotor-stator gap and at the entrance of the stator passage. Considerable oscillations along the mid-passage line may be due to lack of statistical convergence and the combination of many terms. However, an overall decreasing trend towards the exit of the stator appears visible in spite of the noise. This trend indicates that substantial deterministic pressure fluctuations occur within the gap, and at the entrance to the stator passage. These fluctuations are attenuated as the flow exits the stator row

We are presently repeating these measurements, this time using stereo PIV data and a larger database, consisting of 1000 realizations per phase and 40 measured phases for calculating the deterministic parameters.

4.5 High Resolution Data, and Turbulence in the Near Wake

High-resolution measurements are performed using a sample area of 15x15 mm^2 (some with vector spacing of 234 μm in 64x64 maps, and some with spacing of 117 μm in 128x128 vectors maps) and converged statistics is obtained by averaging 1000 data sets. To cover the desired range we match four data sets, all at the same phase. Figure 13 shows the phase-averaged velocity components and vorticity within the rotor wake (setup No. 2). The wake is "discontinuous", i.e. it is kinked at about (0.28-0.58). This kinked region is characterized by concentrated vorticity, elevated turbulent kinetic energy (see Figures 4 and 13), and quadrupole distributions of Reynolds shear stress and mean shear strain (not shown, see Chow et al., 2002a, 2003a, b, c for more details). Consequently, we refer to these regions as "turbulent hot spots". To explain the mechanism generating the hot spots note (as mentioned before) that the chopped off upstream stator wake segments are convected at different speeds along the suction and pressure sides of the rotor blade. When these phase-lagged segments reach the rotor wake, they are no

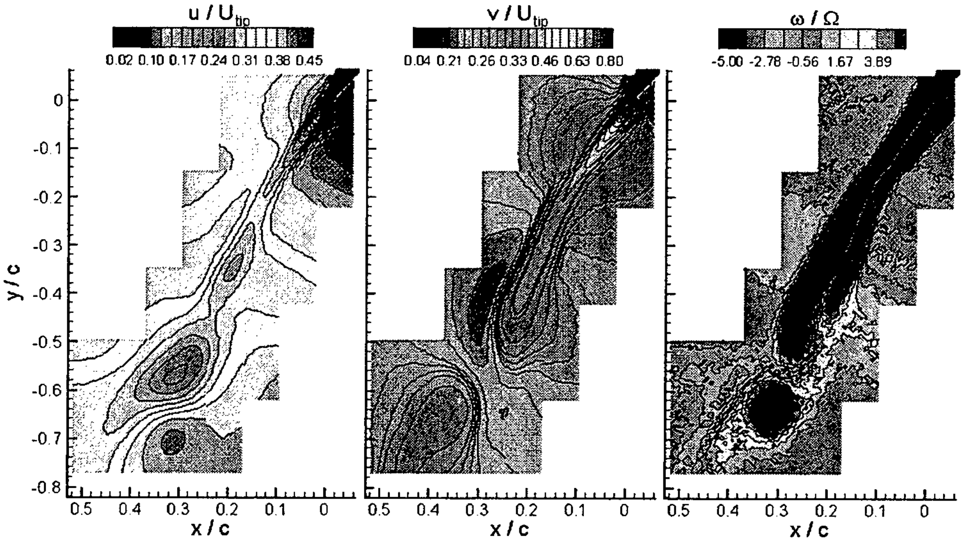

Figure 13. Phase-averaged axial velocity (left), lateral velocity (middle) and vorticity (right) distributions within the rotor wake. The rotor trailing edge is visible at the upper right-hand corner, and the data covers a region up to 90% rotor chord lengths from the trailing edge. U_{tip}=8 m/s, Ω=52.36 rad/s.

longer aligned, creating discontinuities across the rotor wake (e.g. Figures 4 and 13). Upstream of the rotor wake some of the area is occupied by a wake with a low axial velocity (e.g. at y/c=-0.4, Figure 13), and the rest contains fluid with higher axial momentum. Consequently, the rotor wake is sheared.

In this Section we provide sample data on the structure of the turbulence in the near wake including spectra and estimates of dissipation rates. In references Chow et al., 2003a, b, c we also compare the distributions, magnitudes and alignments of measured Reynolds and SGS stresses to the corresponding parameters of the phase-averaged and spatially filtered strain fields. We also examine the effect of stator wake impingement on the production and dissipation of turbulence in the boundary layer. The results identify region and flow phenomena where turbulence modeling could be improved, e.g. the hot spots and sites with strong interactions between an impinging wake and a boundary layer. Conversely, in other regions, e.g. wake segments away from the trailing edge and from the hot spots have the typical structure of turbulent wakes.

One-dimensional turbulence spectra: Several sample lines, which are aligned with the most probable directions of turbulence homogeneity (relative streamlines in this case), are chosen in the wake (Figure 14). Along each line, we calculate and then ensemble average the longitudinal and normal spatial spectra, $E_{11}(k_1)$ and $E_{22}(k_1)$, where k_1 is the wavenumber along the direction of the line. The results are presented as distributions of $E_{11}(k_1)$ and $3/4E_{22}(k_1)$ since they are equal in isotropic turbulence. Details can be found in Doron et al. (2001) and Chow et al. (2003a, b, c). Assuming isotropic, homogeneous turbulence in the inertial range, one can estimate the dissipation rate, ε, and the Kolmogorov scale using (Tennekes & Lumley, 1972)

$$E_{11}(k_1) = (18/55)(1.6)\varepsilon^{2/3}k_1^{-5/3} \qquad\qquad \eta = \left(\nu^3/\varepsilon\right)^{1/4} \qquad (5)$$

Figure 14 shows the lines overlaid on the distributions of turbulent kinetic energy, and the corresponding spectra along with the values of ε and h. In some cases, e.g. near the trailing edge and within the hot spot, the two spectra deviate from each other, indicating strong turbulence anisotropy. It is also hard to find an inertial range with a –5/3 slope in the spectra of turbulence

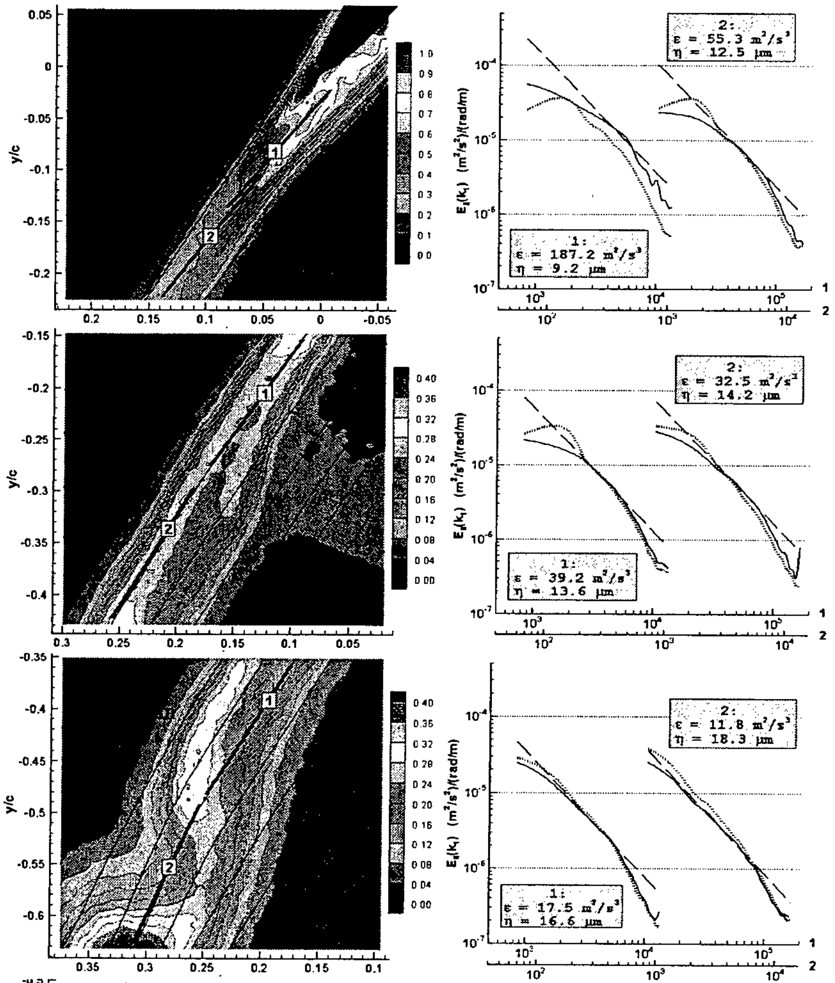

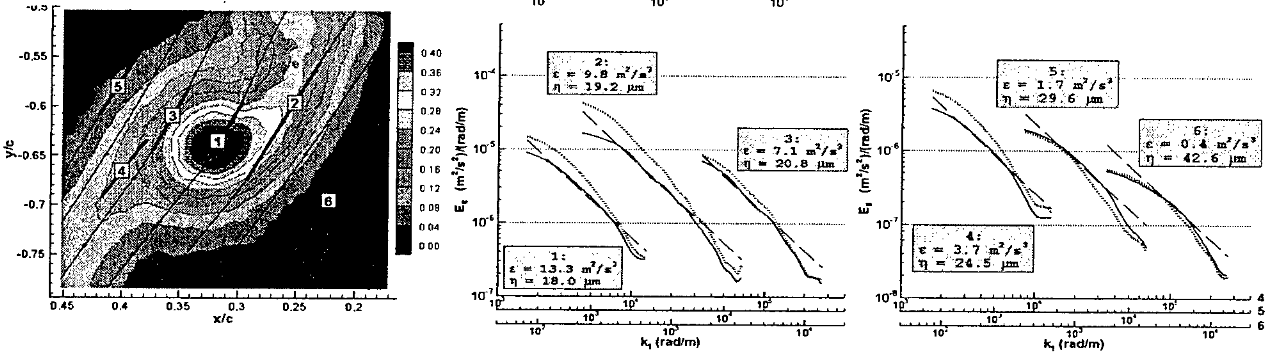

Figure 14. (left) Distributions of turbulent kinetic energy (m^2/s^2) and relative streamlines; and (right) 1-D spatial energy-density spectra along the indicated sample lines. The rotor trailing edge is located at (0,0). Solid line: $E_{11}(k_1)$; dotted line: $3/4\ E_{22}(k_1)$; dashed line: a -5/3 slope line fits to $E_{11}(k_1)$. Estimated dissipation rates and Kolmogorov length scale are presented near each line.

near the trialing edge. However, just a short distance downstream, an inertial range appears and the turbulence appears to be more isotropic. The isotropy persists within and outside of the wake except for the hot spot region.

The values of ε decrease monotonically (except for the hot spot), initially very rapidly, by about 4 times from line 1 to line 2 in the 0-0.26c range, and then more slowly. In the 0.41c-0.70c range, ε is already an order of magnitude lower than the trailing edge level. Near the hot spot ε increases slightly. Outside of the wake the dissipation rates are substantially lower, by 2-3 orders of magnitude, than the values at the trailing edge, and more than one order of magnitude lower than the mid-wake regions. The resulting values of the h also vary. Thus, our fixed vector spacing of 234 µm misses decreasing fractions of the high wave number part of the spectrum with increasing distance from the trailing edge. Interestingly, the integral length scale, estimated from $l = k^{3/2}/\eta$, is 3.3mm for the 0.18c-0.48c region, consistent with the width of the wake there.

Subsequent analysis, described in Chow et al. (2003a) includes also measurements of the distributions of production, a comparison between production and dissipation rates, and the relative alignment between corresponding stress and stain tensors (they are not aligned, in contradiction to the basic assumptions of eddy viscosity models). Chow et al. (2003a) and Soranna et al. (2004) also include detailed measurements in the rotor boundary layer, which examine the effects of stator wake impingement on the momentum thickness and turbulence in the boundary layer. These studies show that wake impingement cause boundary layer thinning, at that the dominant cause is time dependent variations in the pressure field. These studies are still in progress and will be described in detail in future reports.

4.6 SGS energy budget

Large eddy simulation (LES) distinguishes between the large-scale motions and the Sub Grid-Scale (SGS) motions by spatially filtering the velocity field (Leonard, 1974; Piomelli et al., 1991; Meneveau & Katz, 2000). This process introduces the SGS stress tensor,

$$\tau_{ij}^{SG} = \widehat{u_i u_j} - \widehat{u}_i \widehat{u}_j \tag{6}$$

where "$\widehat{\ldots}$" indicates spatial filtering at scale *Δ*. The resolved velocity field, $\widehat{u}_i$, is of interest, not only in the context of LES, but also in studying the dynamics of large-scale motions within the flow. In this section we examine the energy transfer associated with large-scale motions using the near wake data. We use a box filter with size of eight-vector spacing, 1.875 mm. This corresponds to a wavenumber, $2\pi/\Delta=3.35\text{x}10^3$ rad/m, which falls between the inertial range and the integral scale of turbulence, depending on position. The evolution of the *mean resolved kinetic energy*, $K = 0.5\overline{\widehat{u}_i \widehat{u}_i}$, (Piomelli et al., 1991; Meneveau & Katz, 2000), is governed by

$$\frac{\partial}{\partial t} K + \overline{\widehat{u}_j} \frac{\partial}{\partial x_j} K = -(-\overline{\tau_{ij}^{SG} \widehat{S_{ij}}}) - 2\nu \overline{\widehat{S_{ij}} \widehat{S_{ij}}} - \frac{\partial}{\partial x_j} A_{ij} \tag{7}$$

As discussed in Chow et al., (2003c, 2004, in preparation) *K* can be further decomposed to mean resolved kinetic energy and mean resolved turbulent kinetic energy, followed by additional decompositions. This work is still in progress and will be reported on in the future. The first term on the right hand side of Equation 7 is the so-called "SGS dissipation", $\varepsilon_K^{SG} = -\overline{\tau_{ij}^{SG} \widehat{S}_{ij}}$, which describes the energy transfer of from the resolved to the SGS motions. Figure 15 compares a sample distribution of SGS dissipation in the near wake to the filtered production rate $-\overline{\widehat{u}_i{}'\widehat{u}_j{}'}\overline{\widehat{S}_{ij}}$, which represents the energy flux from the resolved mean flow to the resolved turbulence. Both the SGS dissipation and the filtered production have magnitude peaks along two parallel layers on both sides of the rotor wake centerline, consistent with regions with high overall turbulence production (Chow

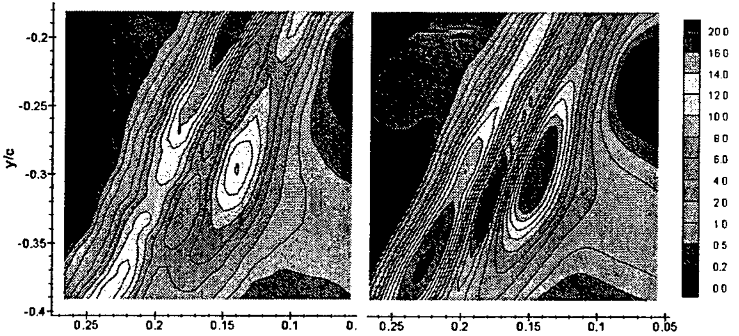

Figure 15: SGS dissipation and production terms (m^2/s^3), 0.18c-0.48c downstream of the rotor trailing edge.

et al., 2003a). However, they clearly peak at different locations. Reasons for the discrepancy are presently being analyzed Chow et al. (2004, in preparation), and will be discussed in future reports. Elevated levels exits also to the right of the rotor wake, where a stator wake segment impinges on the rotor wake. The other data sets have peaks close to the trailing edge and within the hot spot.

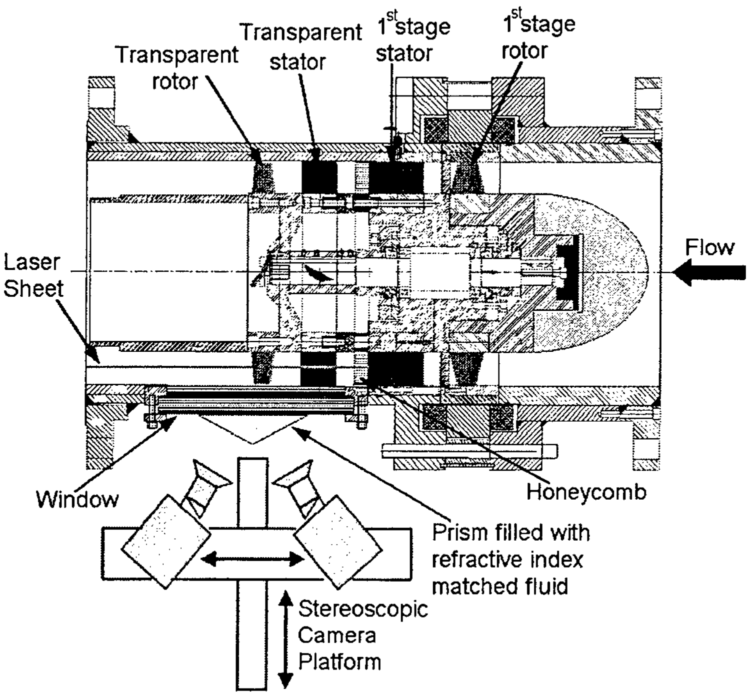

Figure 16: The new stereo-PIV setup

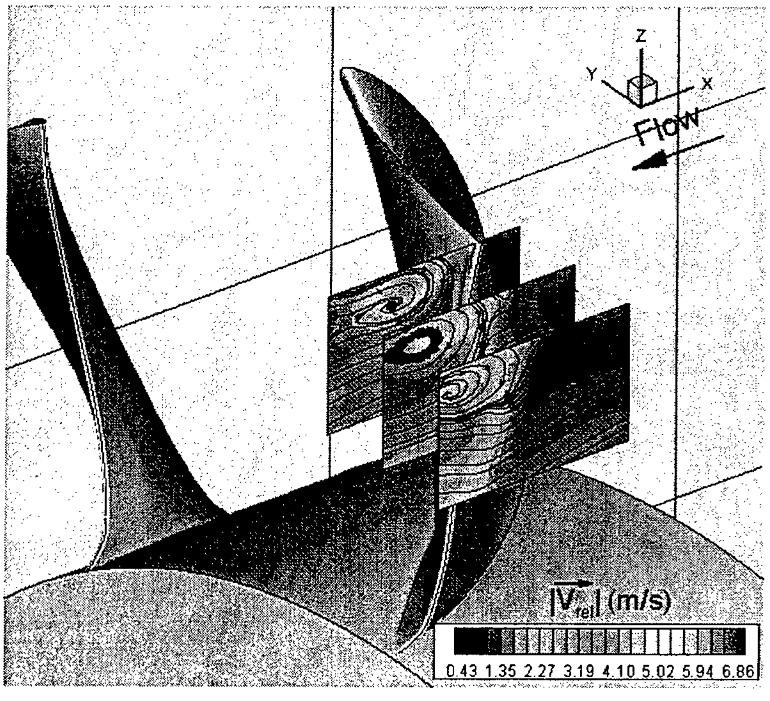

Figure 17: Phase-averaged velocity magnitude (all three components) in the rotor frame of reference (color), along with the absolute streamlines.

5. Future/Present Plans

The research presently in progress will continue over the next two years, and has the following objectives:

a. Measurements and Modeling of Deterministic Stresses in the Tip Region using stereo PIV measurements. The optical setup is illustrated in Figure 16. These measurements substantially extend the scope and resolution of the data obtained to-date in order to obtain a clear picture on the phase-dependent variations in the structure and trajectory of the tip vortex. A sample, recently obtained 3-D phase averaged velocity distribution is presented in Figure 17. Such data is obtained by measuring all three velocity components in closely spaced planes (less than sheet thickness). Also, as noted before, we record 1000 instantaneous realizations in each phase, and obtain data for 40 phases in one blade passage to prevent the need for interpolations.

b. Measurements of vortex strength and trajectory in a plane that is perpendicular to the flow direction.

c. Develop a simplified model for deterministic stresses extending the ideas introduced in (Meneveau & Katz, 2002). RANS simulations of the flow in the rotor and stator passages are presently in progress.

d. Study/measure the effect of spacing between blade rows on the distributions of deterministic Stresses.

e. Measure the effect of tip gap on the tip vortex structure and associated deterministic stresses.

f. Study the structure and dynamics of deterministic stresses, production and dissipation off design conditions, along with their dependence on large-scale instabilities that develop as stall conditions are approached.

g. Measure and analyze the dynamics of SGS stresses, and address SGS stress modeling issues that are unique to flows within turbomachines.

h. Explore the relationships between: (1) Reynolds decomposition using phase averaging, and (2) SGS decomposition in terms of filter scale. Our results so far point to an important role played by the "subgrid part" of the mean flow when the filtering scale becomes comparable with length-scales of significant variations in the mean flow (such as wake thickness).

i. Develop tools to enhance the resolution of the PIV data to vector spacing of about 50 μm. The enhanced spatial resolution is essential for filtering the data in different scales, and for improving the level of the detail that can be obtained in boundary layers and tip gap.

6. Papers published to Date

The following is a list of published/submitted papers on the research performed funded by this program.

Journal Papers

Meneveau, C., Katz, J., (2002), "A Deterministic Stress Model for Rotor-Stator Interactions in Simulations of Passage-Averaged Flow." Journal of Fluids Engineering, Vol. 124, No. 2, pp. 550-554.

Uzol, O., Chow, Y.C., Katz, J., Meneveau, C., (2002a), "Unobstructed PIV measurements within an axial turbo-pump using liquid and blades with matched refractive indices," Experiments in Fluids, Vol. 33, pp. 909-919.

Uzol, O., Chow, Y.C., Katz, J., Meneveau, C., (2002b), Experimental Investigation of Unsteady Flow Field Within a Two Stage Axial Turbomachine Using Particle Image Velocimetry, J. of Turbomachinery, Vol. 124, pp. 542-552.

Chow, Y.C., Uzol, O., Katz, J., (2002a), "Flow Non-Uniformities and Turbulent "Hot Spots" Due To Wake-Blade And Wake-Wake Interactions in a Multistage Turbomachine," J. of Turbomachinery, Vol. 124, pp. 553-563.

Uzol, O., Chow, Y.C., Katz, J., Meneveau, C., (2003a), "Average Passage Flow Field and Deterministic Stresses in The Tip and Hub Regions of A Multi-Stage Turbomachine," J. of Turbomachinery, Vol. 125, pp. 714-725.

Chow, Y.C., Uzol, O., Katz, J., (2003a), "On the Flow and Turbulence Within the Wake and Boundary Layer of A Rotor Blade Located Downstream of an IGV," Submitted for Publication in J. of Turbomachinery.

Full Conference papers

Uzol, O., Chow, Y.C., Katz, J., Meneveau, C., (2001), "Unobstructed PIV Measurements Within an Axial Turbo-Pump Using Liquid And Blades With Matched Refractive Indices," 4th International Symposium on Particle Image Velocimetry, Göttingen, Germany, September 17-19.

Chow, Y.C., Uzol, O., Katz, J., Meneveau, C., (2002b), "An Investigation of Axial Turbomachinery Flows Using PIV in an Optically-Unobstructed Facility," The 9th of International Symposium on Transport Phenomena and Dynamics of Rotating Machinery, Honolulu, Hawaii, February 10-14.

Uzol, O., Chow, Y.C., Katz, J., Meneveau, C., (2002c), Experimental Investigation of Unsteady Flow Field Within a Two Stage Axial Turbomachine Using Particle Image Velocimetry, International Gas Turbine Institute, ASME TURBO EXPO 2002, paper no. GT-2002-30664, Amsterdam, The Netherlands.

Chow, Y.C., Uzol, O., Katz, J., (2002c), "Flow Non-Uniformities and Turbulent "Hot Spots" Due To Wake-Blade And Wake-Wake Interactions in a Multistage Turbomachine," International Gas Turbine Institute, ASME TURBO EXPO 2002, paper no. GT-2002-30667, Amsterdam, The Netherlands.

Uzol, O., Chow, Y.C., Katz, J., Meneveau, C., (2003b), "Average Passage Flow Field and Deterministic Stresses in The Tip and Hub Regions of A Multi-Stage Turbomachine," International Gas Turbine Institute, ASME TURBO EXPO 2003, paper no. GT-2003-38598, June 16-19, Atlanta GA.

Chow, Y.C., Uzol, O., Katz, J., (2003b), "On the Flow and Turbulence Within the Wake and Boundary Layer of A Rotor Blade Located Downstream of an IGV," International Gas Turbine Institute, ASME TURBO EXPO 2003, paper no. GT-2003-38599, June 16-19, Atlanta GA.

Chow, Y.C., Uzol, O., Katz, J., Meneveau, C., (2003c), "Experimental Study of The Structure of a Rotor Wake in a Complex Turbomachinery Flow," 4TH ASME_JSME Joint Fluids Engineering Conference, Honolulu, Hawaii, USA, July 6-11 (Proceedings of FEDSM-2003), paper No. FEDSM-2003-45575.

Soranna, F., Chow, Y.C., Uzol, O., Katz, J., (2004), "ROTOR boundary layer response to an impinging wake," paper No. HT-FED2004-56125, Proceedings of HT/FED'04, 2004 Heat Transfer/Fluids Engineering Summer Conference, July 11-15, Charlotte, North Carolina.

Uzol, O., Chow, Y.C., Soranna, F., Katz, J., Meneveau, C., (2004a), "3-D Measurements of Deterministic Stresses within a Rotor-stator Gap at Mid Span and Tip Regions," paper No. HT-FED2004-56513, Proceedings of HT/FED'04, 2004 Heat Transfer/Fluids Engineering Summer Conference, July 11-15, Charlotte, North Carolina.

Uzol, O., Chow, Y.C., Soranna, F., Katz, J., (2004b), "3D Structure of a Rotor Wake at Mid-span and Tip Regions," Paper No. AIAA-2004-2552, 34th AIAA Fluid Dynamics Conference and Exhibit, Portland, Oregon, June 28 - July 1.

References:

Adamczyk J. J., 1996, "Wake Mixing in Axial Flow Compressors," ASME Paper No. 96-GT-029

Adamczyk J.J., Mulac R.A., Celestina M.L., 1986, "A Model for Closing the Inviscid Form of the Average-Passage Equation System," ASME Paper No. 86-GT-227

Adamczyk J.J.; Celestina M.L.; Beach T.A.; Barnett M., 1990, "Simulation Of Three Dimensional Viscous Flow Within A Multistage Turbine," ASME J. of Turbomachinery, 112, p. 370

Adamczyk, J. J., 1985, "Model Equation for Simulating Flows in Multistage Turbomachinery," ASME Paper No. 85-GT-226.

Balzani N., Scarano F., Riethmuller M. L., Breugelmans F. A. E., 2000, "Experimental Investigation of the Blade-to-Blade Flow in a Compressor Rotor by Digital Particle Image Velocimetry," ASME J. of Turbomachinery, Vol. 122, pp. 743-750.

Bouda, N. N., Benabid, T., Fulachier, L., 2002, "Relaxation of turbulent boundary layer submitted to sudden distortion at the wall," AIAA Journal, Vol. 40, No. 1, pp. 58-66.

Busby J.; Sondak D.; Staubach B.; Davis R., 2000, "Deterministic Stress Modeling of a Hot Gas Segregation in a Turbine," J. of Turbomachinery 122, 62.

Chen,

Chow, Y.C., Uzol, O., Katz, J., (2002a), "Flow Non-Uniformities and Turbulent "Hot Spots" Due To Wake-Blade And Wake-Wake Interactions in a Multistage Turbomachine," J. of Turbomachinery, Vol. 124, pp. 553-563.

Chow, Y.C., Uzol, O., Katz, J., (2002c), "Flow Non-Uniformities and Turbulent "Hot Spots" Due To Wake-Blade And Wake-Wake Interactions in a Multistage Turbomachine," International Gas Turbine Institute, ASME TURBO EXPO 2002, paper no. GT-2002-30667, Amsterdam, The Netherlands.

Chow, Y.C., Uzol, O., Katz, J., (2003a), "On the Flow and Turbulence Within the Wake and Boundary Layer of A Rotor Blade Located Downstream of an IGV," Submitted for Publication in J. of Turbomachinery.

Chow, Y.C., Uzol, O., Katz, J., (2003b), "On the Flow and Turbulence Within the Wake and Boundary Layer of A Rotor Blade Located Downstream of an IGV," International Gas Turbine Institute, ASME TURBO EXPO 2003, paper no. GT-2003-38599, June 16-19, Atlanta GA.

Chow, Y.C., Uzol, O., Katz, J., Meneveau, C., (2002b), "An Investigation of Axial Turbomachinery Flows Using PIV in an Optically-Unobstructed Facility," The 9th of International Symposium on Transport Phenomena and Dynamics of Rotating Machinery, Honolulu, Hawaii, February 10-14.

Chow, Y.C., Uzol, O., Katz, J., Meneveau, C., (2003c), "Experimental Study of The Structure of a Rotor Wake in a Complex Turbomachinery Flow," 4TH ASME_JSME Joint Fluids Engineering Conference, Honolulu, Hawaii, USA, July 6-11 (Proceedings of FEDSM-2003), paper No. FEDSM-2003-45575.

Doron, P., Bertuccioli, L., Katz, J., Osborn, T. R., 2001, "Turbulence characteristics and dissipation estimates in the costal ocean bottom boundary layer from PIV data," Journal of Physical Oceanography, Vol. 31, pp. 2108-2134.

Gogineni, S. Goss, L., Copenhaver, W., and Gorrell, S., 1997, "Development of Digital Two-Color PIV for turbomachinery applications," AIAA Paper No. 97-0494.

He, L., Chen, T., Wells, R. G., Li, Y. S., Ning, W., 2002, "Analysis of rotor-rotor and stator-stator interferences in multi-stage turbomachines," ASME *Journal of Turbomachinery,* Vol. 124, pp. 564-571.

Ho, Y.H., Lakshminarayana, B., 1995, "Computation of unsteady viscous flow through turbomachinery blade row due to upstream rotor wakes," ASME, J. TURBOMACHINERY, Vol. 117 (4), pp. 541-552.

Lakshminarayana, B. 1991 An Assessment Of Computational Fluid Dynamic Techniques In The Analysis And Design Of Turbomachinery - 1990 Freeman Scholar Lecture. *J. Of Fluids Eng,* 113, 315.

Lejambre C.R.; Zacharias R.M.; Biederman B.P.; Gleixner A.J.; Yetka C.J., 1998, "Development And Application Of A Multistage Navier-Stokes Solver. Part II: Application To A High Pressure Compressor Design," ASME J. Turbomachinery 120, 215.

Leonard, A., 1974, "Energy Cascade in Large-Eddy Simulations of Turbulent Fluid Flows," Adv. Geophys. 18:237

Lesieur, M. & Metais, O. 1996 New Trends In Large-Eddy Simulations Of Turbulence. *Annu. Rev. Fluid Mech.*, 28, 45--82.

Liu, S., Katz, J., Meneveau, C., 1999, "Evolution And Modeling of Subgrid Scales During Rapid Straining of turbulence", Journal of Fluid Mechanics, Vol. 387, pp. 281 - 320.

Liu, S., Meneveau, C., Katz, J., 1994, "On the Properties of Similarity Subgrid-Scale Models as Deduced from Measurements in a Turbulent Jet," J. Fluid Mech., Vol 275, pp. 83-119.

Liu, S., Meneveau, C., Katz, J., 1995, "Experimental Study of Similarity Subgrid-Scales Models of Turbulence in The Far Field of a Jet", Journal of Applied Scientific Research, Vol. 54, pp. 177-190.

Meneveau C., Katz J., 2002, "A Deterministic Stress Model for Rotor-Stator Interactions in Simulations of Average-Passage Flow," Journal of Fluids Engineering, Vol. 124, pp. 550-554.

Meneveau, C. 1993 Statistics of turbulence subgrid-scale stresses: Necessary conditions and experimental tests *Phys. Fluids A* 6 815.

Meneveau, C., Katz, J., 2000, "Scale-Invariance and Turbulence Models for Large-Eddy Simulation," Annu. Rev. Fluid Mech. Vol. 32, pp. 1-32.

O'Neil, J. & Meneveau, C 1997 Subgrid-Scale Stresses And Their Modeling In The Turbulent Plane Wake, *J. Fluid Mech.*, 349, 253.

Piomelli, U., Cabot, W. H., Moin, P., Lee, S., 1991, "Subgrid-Scale Backscatter in Turbulent and Transitional Flows," Phys. Fluids A, 3:1766-71.

Prato, J., Lakshminarayana B., Suryavamshi N., 1997, "Exit Flow Field of an Embedded Stator in a Multi-Stage Compressor," J. of Propulsion and Power, Vol. 13 No. 2, pp. 169-177.

Prato, J., Lakshminarayana B., Suryavamshi N., 1998, "Steady and Unsteady Three-Dimensional Flow Field Downstream of an Embedded Stator in a Multi-Stage Axial Flow Compressor Part I: Unsteady Velocity Field," ASME Paper No. 98-GT-521

Rai, M.M. 1987 Navier-Stokes Simulation Of Rotor/Stator Interaction Using Patched And Overlaid Grids. *J. Of Propulsion And Power*, 3, 387.

Rhie C.M.; Gleixner A.J.; Spear D.A.; Fischberg C.J.; Zacharias R.M., 1998 "Development and Application Of A Multistage Navier-Stokes Solver. Part I: Multistage Modeling Using Body Forces and Deterministic Stresses, " ASME J. Turbomachinery 120, p. 205.

Rogallo, R. & Moin, P. 1984 Numerical Simulation Of Turbulent Flows. *Ann. Rev. Fluid. Mech.,* 16, 99.

Roth, G. I., and Katz, J., 2001, "Five Techniques for Increasing the Speed and Accuracy of PIV Interrogation," Meas. Sci. Technol. 12, pp. 238-245.

Roth, G. I., Mascenik, D. T., and Katz, J., 1999, "Measurements of The Flow Structure and Turbulence Within A Ship Bow Wave," Physics of Fluids, **11**, No. 11, pp. 3512-3523.

Sanders A.J., Papalia J., Fleeter S., 2002, "Multi-Blade Row Interactions in a Transonic Axial Compressor: Part I-Stator Particle Image Velocimetry (PIV) Investigation," ASME J. of Turbomachinery, Vol. 124, pp. 10-18.

Sinha, M., and Katz, J., 2000, "Quantitative Visualization of the Flow in a Centrifugal Pump With Diffuser Vanes-I: On Flow Structures and Turbulence," ASME J. Fluids Eng., 122, pp. 97-107.

Sinha, M., Katz, J., and Meneveau, C., 2000, "Quantitative Visualization of the Flow in a Centrifugal Pump With Diffuser Vanes-II: Addressing Passage-Averaged and Large-Eddy Simulation Modeling Issues in Turbomachinery Flows," ASME J. Fluids Eng., 122, pp. 108-116.

Sinha, M., Pinarbasi, A., Katz, J., 2001, "The Flow Structure During Onset and Developed States of Rotating Stall Within a Vaned Diffuser of a Centrifugal Pump," Journal of Fluids Engineering, Vol. 123, No. 3, pp. 490-499.

Smith L. H. Jr., 1966, "Wake Dispersion in Turbomachines," Journal of Basic Engineering, September 1966, pp. 688-690.

Soranna, F., Chow, Y.C., Uzol, O., Katz, J., (2004), "ROTOR boundary layer response to an impinging wake," paper No. HT-FED2004-56125, Proceedings of HT/FED'04, 2004 Heat Transfer/Fluids Engineering Summer Conference, July 11-15, Charlotte, North Carolina.

Speziale, C. 1991 Analytical methods for the development of Reynolds-stress closures in turbulence, *Ann. Rev. Fluid Mech.* **23**, 107.

Sridhar, G., Katz, J., (1995), "Lift and Drag Forces on Microscopic Bubbles Entrained by a Vortex", Physics of Fluids, Vol. 7, No. 2, pp. 389-399.

Suryavamshi N., Lakshminarayana B., Prato J., 1998, "Steady and Unsteady Three-Dimensional Flow Field Downstream of an Embedded Stator in a Multi-Stage Axial Flow Compressor Part II: Composite Flow Field," ASME Paper No. 98-GT-522

Suryavamshi N., Lakshminarayana B., Prato J., 1998, "Steady and Unsteady Three-Dimensional Flow Field Downstream of an Embedded Stator in a Multi-Stage Axial Flow Compressor Part III: Deterministic Stress and Heat Flux Distribution and Average-Passage Equation System," ASME Paper No. 98-GT-523

Tao, B., Katz, J., Meneveau, C., 2000, "Geometry and Scale Relationships in High Reynolds Number Turbulence Determined From 3-D Holographic Velocimetry," Physics of Fluids Journal, Vol. 12, No. 5, pp. 941-944.

Tao, B., Katz, J., Meneveau, C., 2002, "Holographic PIV Measurements of the Structure of SGS Stress Eigenvectors and their alignment Relative to Parameters Based on the Filtered Velocity Gradients," Journal of Fluid Mechanics, Vol. 457, pp. 35-78.

Tennekes, H., Lumley, J. L., 1972, "A first course in turbulence," The MIT Press.

Tisserant D., Breugelmans F.A.E., 1997, "Rotor Blde-to-Blade Measurements Using Particle Image Velocimetry," ASME J. of Turbomachinery, 119, pp. 176-181.

Uzol, O., Chow, Y.C., Katz, J., Meneveau, C., (2001), "Unobstructed PIV Measurements Within an Axial Turbo-Pump Using Liquid And Blades With Matched Refractive Indices," 4th International Symposium on Particle Image Velocimetry, Göttingen, Germany, September 17-19.

Uzol, O., Chow, Y.C., Katz, J., Meneveau, C., (2002a), "Unobstructed PIV measurements within an axial turbo-pump using liquid and blades with matched refractive indices," Experiments in Fluids, Vol. 33, pp. 909-919.

Uzol, O., Chow, Y.C., Katz, J., Meneveau, C., (2002b), Experimental Investigation of Unsteady Flow Field Within a Two Stage Axial Turbomachine Using Particle Image Velocimetry, J. of Turbomachinery, Vol. 124, pp. 542-552.

Uzol, O., Chow, Y.C., Katz, J., Meneveau, C., (2002c), Experimental Investigation of Unsteady Flow Field Within a Two Stage Axial Turbomachine Using Particle Image Velocimetry, International Gas Turbine Institute, ASME TURBO EXPO 2002, paper no. GT-2002-30664, Amsterdam, The Netherlands.

Uzol, O., Chow, Y.C., Katz, J., Meneveau, C., (2003a), "Average Passage Flow Field and Deterministic Stresses in The Tip and Hub Regions of A Multi-Stage Turbomachine," J. of Turbomachinery, Vol. 125, pp. 714-725.

Uzol, O., Chow, Y.C., Katz, J., Meneveau, C., (2003b), "Average Passage Flow Field and Deterministic Stresses in The Tip and Hub Regions of A Multi-Stage Turbomachine," International Gas Turbine Institute, ASME TURBO EXPO 2003, paper no. GT-2003-38598, June 16-19, Atlanta GA.

Uzol, O., Chow, Y.C., Soranna, F., Katz, J., (2004b), "3D Structure of a Rotor Wake at Mid- span and Tip Regions," Paper No. AIAA-2004-2552, 34th AIAA Fluid Dynamics Conference and Exhibit, Portland, Oregon, June 28 - July 1.

Uzol, O., Chow, Y.C., Soranna, F., Katz, J., Meneveau, C., (2004a), "3-D Measurements od Deterministic Stresses within a Rotor-stator Gap at Mid Span and Tip Regions," paper No. HT-FED2004-56513, Proceedings of HT/FED'04, 2004 Heat Transfer/Fluids Engineering Summer Conference, July 11-15, Charlotte, North Carolina.

Van de Wall A.G., Kadambi J.R., Adamczyk J.J., 2000, "A Transport Model for the Deterministic Stresses Associated With Turbomachinery Blade Row Interactions," ASME J. of Turbomachinery, 122, pp. 593-603.

Van Zante D. E., Adamczyk J. J., Strazisar A. J., Okiishi T. H., 2002, "Wake Recovery Performance Benefit in a High-Speed Axial Compressor," ASME J. of Turbomachinery, Vol. 124, pp. 275-284.

Wernet, M. P., 2000, "Development of Digital Particle Imaging Velocimetry for use in Turbomachinery", Experiments in Fluids, 28, pp. 97-115.

Wilcox, D.C. 1993, Turbulence Modeling for CFD (*DCW Industries, Inc.*, La Canada, CA 91011)

Zhang, J., Tao, B. & Katz, J. 1997 Turbulent Flow Measurement In A Square Duct With Hybrid Holographic PIV, *Experiments In Fluids* **23**, 373.